ABSTRACT

Title of dissertation: CHARACTERIZATION OF MECHANICAL
PROPERTIES AND DEFECTS OF
SOLID-OXIDE FUEL CELL MATERIALS

Patrick Owen Stanley
Doctor of Philosophy, 2018

Dissertation directed by: Professor Eric D. Wachsman
Materials Science and Engineering

Solid-oxide fuel cells (SOFC) have the potential to help the energy economy transition to a more efficient generation method. A challenge in SOFCs is that the composite ceramic cell must maintain a gas-tight seal between the anode and cathode while minimizing the thickness to improve performance. This seal must withstand heating and changes in oxygen content, which affect the physical and mechanical properties of the materials. To understand these effects, it is needed to investigate the effects of environment, microstructure, and macrostructure interplay on the cell's strength, modulus, and fracture toughness.

The mechanical properties of SOFC materials are difficult to study at operating conditions. Most research to date have investigated the material properties at ambient conditions after cycling a cell or at elevated temperatures in air. As part of this work, an enclosed three point bend apparatus has been built which can be heated to the same temperature and environment as an operating SOFC, measuring their properties in situ.

With this technique, among others, a variety of materials and systems have been characterized, including established materials, nickel-oxide and gadolinium doped ceria, to new materials such as a strontium iron cobalt molybdenum oxide. It has been determined how the choice of pore former effects the strength up to elevated temperatures, how fracture toughness and strength can increase with temperature due to relaxation of intrinsic stresses, the most likely time for failure of an SOFC is under reduction due to uniform growth of microstructure flaws and how cell orientation does not impact mechanical properties.

This new knowledge into the changing mechanical properties of the different materials and structures tested will allow for the design and optimization of SOFC devices to maximize reliability and performance. In addition, the apparatus built to measure in-situ properties can also be applied to other temperatures and gaseous environments for different applications. This work helps bring SOFCs from a theoretical lab-based technology to a reliable means of efficient energy generation for use by society.

CHARACTERIZATION OF STRENGTH AND MECHANICAL PROPERTIES OF SOLID-OXIDE FUEL CELL MATERIALS

by

Patrick Owen Stanley

Dissertation submitted to the Faculty of the Graduate School of the
University of Maryland, College Park in partial fulfillment
of the requirements for the degree of
Doctor of Philosophy
2018

Advisory Committee:
Professor Eric D. Wachsman: *Advisor, Chair*
Professor Abhijit Dasgupta: *Dean's Representative*
Professor Isabel K. Lloyd
Professor Lourdes Salamanca-Riba
Professor Sreeramamurthy Ankem

Dedication

I dedicate this to my wife, Bethany, who has encouraged and supported me throughout the process, and to my two wonderful daughters, Lucy and Madeleine. You brighten my life in ways I cannot begin to explain.

Acknowledgments

I would like to start off by thanking my graduate advisor, Dr. Eric Wachsman, for his support during my graduate career. He allowed me the freedom to direct the details of my research and the support to help me reach my goals. He was also supportive of me when my family began to grow through marriage and children, allowing me to continue to develop my personal life while pursuing my degree.

More thanks than I can express is due to my wonderful wife, Bethany and now our daughters, Lucy and Madeleine. When Bethany and I first met, I was still deciding between gradate programs, and now, after many life changes, she continues to challenge and support me in my endeavors. Lucy and Madeleine have provided me with impetus to continue pushing through the challenges and to strike a balance between my personal and professional pursuits.

Of course I owe acknowledgement to my parents, Jim and Marilyn Stanley, who raised me to be inquisitive and persistent. Thank you for helping me to become the person that I am.

The Materials Science and Engineering Department here at UMD has been filled with marvelous and helpful people. Dr. Kathleen Hart was one of the first people I met in the department, seeming to help organize everything, always being there when needed. She has been sorely missed this past year and I hope she is making the most of her retirement. Kay Morris and Jenna Bishop in the business office help the department run smoothly, if it be answering benefits and procurement questions, or doting on my children when they visited. Then of the many professors

I have been able to interact with, I would like to especially thank Dr. Isabel Lloyd who has graciously given me her advice, help make introductions, and passed along opportunities to me when they come her way.

Somehow a small group of my friends of undergraduate have accumulated in the area. It has been a blessing to have them near by, always willing to help out when need be or to just spend time with each other. Dave and Katie Shahin are a large part of what brought me to the University and it has been a blast to go through the program with Dave. Andrew Dunkman has helped me in so many ways, from apartment hunting a thousand miles away to programming questions, for which I express my thanks. And finally, Angela Rudolph has been very supportive of me and my family getting through graduate school.

I owe a good amount of thanks to the various people in lab who helped show me the way to get started with my experiments, allowed me to bounce ideas off them, or helped with the work. Chris Pellegrinelli and Greg Hitz, you were two people who I was always comfortable with going to and asking what seemed like the most basic questions on how to do things, helping me get started in lab. Mohammad Hussain and Yi-Lin Huang shared their experience and knowledge of material science as I worked through the fundamentals. Thanks to Tom Hays for being my partner as we started mechanical testing in lab. Ian Robinson, Evans Gritton and Jon O'Neill provided much needed help with SEM, XRD, and modeling, saving me from fumbling through it myself.

I would like to acknowledge my friends and classmates at the University who formed part of my support network, sharing knowledge and encouragement. Mimi

Table of Contents

List of Tables

viii

List of Figures

List of Abbreviations and Symbols

Chapter 1: Introduction

1.1 Motivation for Solid-Oxide Fuel Cell Research

The world depends on fossil fuels for its daily energy needs. This is a fact that is going to stay with us for the foreseeable future. By 2040, it is estimated that fossil fuels will still supply 78% of total energy demand. [1] Traditionally, the annual increase in demand is met by an increase in supply of fuel. This increase is supplied by developments in mining and drilling operations, although recent advances have been found to be controversial, such as hydraulic fracturing. [2,3] These concerns do not even account for the increased emissions caused from combustion of fossil fuels and their effect on the global environment. [4–6]

An alternative to increasing the supply and usage of fossil fuels is to increase our efficiency of turning the fuel into useful work. Solid-oxide fuel cells (SOFCs) have the ability to solve this for applications where electrical power is desired. SOFCs allow for the direct conversion of chemical energy to electrical energy, whereas devices such as combustion generators must convert chemical energy to thermal energy, to mechanical energy, and finally to electrical energy. Each energy conversion has intrinsic losses, limiting efficiency. Power generation plants have efficiencies around 30%, while a stand-alone SOFC generator can convert fuel to electricity at 45 to 65%

efficiency. [7,8] SOFCs are able to run on a variety of fuel sources, such as hydrogen, methane or even biogas. [9,10] This fuel flexibility and higher efficiency positions SOFCs to bridge the gap in the energy economy as it transitions from fossil fuels to renewable sources. However, many technical hurdles still remain which currently limit SOFCs' viability and must be addressed.

1.2   Solid-Oxide Fuel Cell Operation

Figure 1.1 demonstrates how a hydrogen fueled SOFC operates. Fuel is exposed to the anode side of the cell, while an oxygen rich gas (usually air) is exposed to the cathode side. Separating the two sides is the cell itself, with anode, electrolyte, and cathode. The electrolyte is only conductive to oxygen ions, not electrons. At the cathode, diatomic oxygen gas will disassociate into oxygen ions, each with a $2-$ charge from the addition of electrons to the oxygen. The oxygen ions then travel though the electrolyte and react with the fuel at the anode side, freeing the previously captured electrons. To maintain charge balance, electrons must travel in the opposite direction, to the cathode. Because the electrolyte only allows oxygen ions to diffuse though it, the electrons travel though an external circuit performing useful work in the process.

SOFC materials rely on ionic conduction to transport oxygen from the cathode to the anode. In ionic conduction, oxygen ions hop from site to site via oxygen vacancies, locations where an oxygen atom is missing from the lattice. Because conduction depends on vacancies, the more vacancies in the lattice, the more available
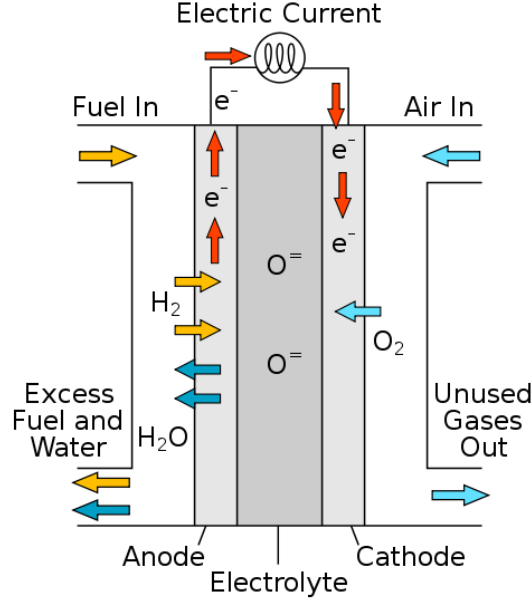
Figure 1.1: Diagram showing flow of materials in the operation of a SOFC. [11]

sites for oxygen to move between, the greater the conductance, and the greater power output of an cell. The relationship between oxygen vacancy concentration and oxygen conductance is given by Equation 1.1, where σ_i is the ionic conductivity, $[V_O^{\bullet\bullet}]$ is the concentration of oxygen vacancies in the lattice, μ_O is the ionic mobility of the oxygen, and Z_e is the charge of the conducting species. [12] Thus, by adding more oxygen vacancies to the system the ionic conductivity increases, but changes in point defect concentrations can have other effects on the materials.

$$\sigma_i = [V_O^{\bullet\bullet}]Ze\mu_O \tag{1.1}$$

During operation, oxygen vacancies are created by exposing the anode to an environment with a low partial pressure of oxygen (pO_2), as shown in Equation 1.2. The oxygen on the surface of the anode side reacts with the fuel to prevent the

3

oxygen from reincorporating into the material. The final concentration of oxygen defects will depend on the exact environmental and material conditions and location in the cell, but some steady state value will eventually be reached.

$$O_O^\times \longleftrightarrow \frac{1}{2} O_2 + V_O^{\bullet\bullet} + 2\,e'$$
(1.2)
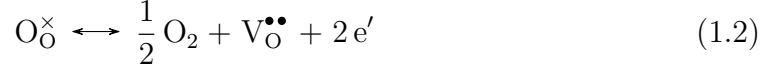
With one side of the cell exposed to low pO_2, and the other side exposed to air, a chemical potential gradient is established across the cell. This gradient drives the motion of oxygen through the cell and generates the electric current. The electrical potential at open circuit conditions is expressed by the Nernst equation, given in Equation 1.4 for the reaction given in Equation 1.3, where f_A is the fugacity of species A, E^o is the standard potential for the reaction, and n is the number of charges involved in the reaction, R is the ideal gas constant and F is Faraday's constant. [13] Commonly, the fugacity is replaced by the partial pressure of the species. For the case of a hydrogen fueled SOFC, Equation 1.4 can be simplified to Equation 1.5. [14] From these equations it can be seen that the partial pressures of the involved species have a large role to play in the open circuit voltage of the cell.

$$aA + bB \longleftrightarrow cC + dD$$
(1.3)

$$E = E^o - \frac{RT}{nF} \ln \left(\frac{f_C^c f_D^d}{f_A^a f_B^b} \right)$$
(1.4)

$$E = E^o + \frac{RT}{2F} \ln \left(\frac{p_{H_2} (p_{O_2})^{1/2}}{p_{H_2O}} \right)$$
(1.5)

For the SOFC to efficiently function, gas must be able reach the active sites in the cell. These active sites, or triple phase boundaries (TPB), are the points where gas, electronic conductor, and ionic conductor meet, as demonstrated in Figure 1.2.
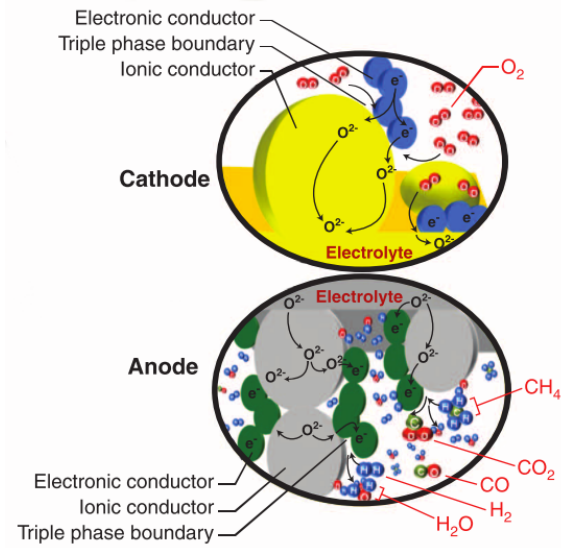
Figure 1.2: Diagram showing the triple phase boundary and the importance as being the site where incorporation and reactions occur. [7]

The more TPB that are present, the more exchange can occur between the gas and the cell at any given time and the current output of the cell is increased. To maximize TPBs, pores can be added, greatly increasing the available surface area of the electrodes. This added porosity does not come without its disadvantages, becoming a trade off between cell performance and mechanical strength. [15, 16]

The cathode and anode materials must facilitate the incorporation of oxygen into the cell and the reaction between the oxygen and the fuel. Typically, the cell operates at temperatures ranging from 600 °C to 1000 °C depending on the technology used in order to increase the ionic conductivity and performance. It is critical that the fuel and air remain separated by the cell. If there is a leak either through the cell or around it, then the electric potential across the cell will decrease leading to failure.

1.3   Solid-Oxide Fuel Cell Materials

Each component of a SOFC is fabricated from a single material or from combinations of materials designed to optimize that parts function. For example, a cell can be comprised of a nickel metal-gadolinium doped ceria (GDC) anode, a GDC electrolyte, and then a lanthanum strontium manganite (LSM) cathode. [17,18] These individual components are cast into thin flexible sheets (tapes) from bulk powders, with additives such as pore formers where appropriate, and then laminated together and fired to create a single cell. As a result, a completed cell has distinct layers in it where the materials and its overall properties abruptly change. This composite structure can then have inter-diffusion between layers, smoothing out the abrupt changes, but creating new structures and compositions that were not present upon lamination. [19]

Nickel has traditionally been used as an anode material in SOFCs, due to its high conductivity and catalytic properties in combination with an ionic conductor such as GDC. A challenge with nickel is that at ambient conditions it oxidizes into nickel oxide, but at operating conditions it reduces to the desired nickel metal. There is a large lattice parameter change between nickel and nickel oxide, so that as it reduces, it decreases volume by over 15%. This means that the overall porosity of the anode layer increases as the SOFC is put into service. [20,21] This increased porosity can greatly decrease the flexural strength and modulus of the anode and of the overall cell. [22,23] Additionally, nickel is prone to poisoning from sulfur contaminants in the fuel, so alternative anodes are of interest for use in SOFCs.

New materials are being developed to serve the various functions within the cell. A first approach has been to develop other metal-ceramic systems to serve the function of the anode. These have included copper, cobalt, and platinum systems, but each suffer from a significant drawback such as coking, long-term performance degradation or cost. A different approach is to use an all-ceramic anode, made of a mixed ionic-electronic conductor (MIEC). Perovskite materials have lead the field in developing an all-ceramic anode, with a transition metal occupying the octahedral B-site. Examples of MIEC ceramics are $La_{1-x}Sr_xCr_{1-y}Mn_yO_3$, $Sr_{0.94}Ti_{0.9}Nb_{0.1}O_{3-\delta}$, $Ba_{0.98}La_{0.02}SnO_3$, or Sr_2MgMoO_6. [24–30]. Due to the all-ceramic nature of these anodes, their thermal expansion coefficients better match that of the other ceramic components of the cell, reducing sintering stresses and improving redox cycling durability, but they tend to have lower conductivity and catalytic performance.

As mentioned previously, GDC, is one of two common choices for electrolyte materials. The other, more traditionally used is yttria-stabilized zirconia (YSZ). YSZ is very stable, has a ratio of ionic conductivity to electronic conductivity (transference number) near 1, and good conductivity at temperatures in excess of 800 °C. At lower temperatures GDC has more conductivity, but does suffer from a lower transference number, especially under extremely reducing conditions. Other rare-earth doped cerias have been used as electrolytes, but GDC tends to outperform them under a variety of conditions. As SOFC operating temperatures are reduced for improved efficiency, GDC becomes the favorable electrolyte and material used in anode composites.

Various cathode materials exist which assist in the incorporation of oxygen

into the lattice. Lanthanum strontium manganite (LSM) is one of the most common. The cathode does not tend to play a structural role in the fabrication of a cell, and thus is not investigated or developed in this work.

1.4 Mechanical Properties

Ideally, an SOFC is as thin as possible to minimize diffusion path lengths and resistances in the cell. [31] Realistically, the cell must be able to withstand the stresses of being manufactured, sealed, heating, and use. This means that a compromise must be met as to how the cell is supported and which components do the supporting. Traditionally, electrolyte supported cells were used with yittra-stabilized zirconia electrolytes, but recently anode supported cells have been able to provide lower resistances while adequately supporting the cell. [32, 33] Now the anode layer, which is needed to the porous for gas diffusion, must support the majority of the stresses the cell is subjected to.

Materials fail when the applied stresses exceed the strength. In a homogeneous material, stresses are applied uniformly throughout the material. In practice, defects will exist in the material creating points of inhomogeneities. These could be intentional with pores which are added to the material or unintended flaws such as inclusions, contamination or grain agglomeration. These microstructural flaws are locations where stresses are concentrated and lead to the ultimate failure of the material.

Stresses are concentrated most by large, sharp featured flaws. As a result, in a

uniform stress field, the largest flaw will usually cause failure. Ceramic materials will tend to fail where the sample is under tensile load and at a location near the point of maximum applied stress. Samples, even if processed together from the same raw materials, will each have a random sampling of flaws from the total batch, and a particular one which causes failure. No matter the care and attention paid to processing, some distribution of flaws will exist. The analysis of the distribution of flaws from a batch of samples is knows as Weibull analysis and is explained in detail in Appendix A.2. To perform Weibull analysis a large number of samples must be tested, but as a result the overall distribution of flaws can be obtained. This allows for the observation of the flaw distribution and if it changes at different points or if another phenomenon is occurring.

Many of the materials used in SOFC have crystal structures which promote the generation of oxygen vacancies. As oxygen vacancies are produced, the interatomic bonding of the structure changes, which can change bulk properties of the crystal. [34, 35] If the strength of the atomic bonds weakens on average, due to added vacancies, it then follows that the elastic modulus and fracture toughness of the crystal would also decrease. This relationship has been shown to fit for single grains of GDC, but this does not necessarily hold true for an actual cell. [36] Grain boundaries can play a large role in the mechanical properties of a bulk sample. For this reason microstructure combined with environmental conditions can play a large role on the overall mechanical properties of a fuel cell.

The first external stress to the cell, and the one most likely to result in failure, comes from the sealing of an individual cell into a stack, creating a gas tight seal

9

between the anode and cathode sides. While it is a compressive force that is applied, the cells are never perfectly flat, resulting in a flexural stresses as the cell is pressed flat. It is for this reason that the study of the failure of SOFC materials utilizes flexural testing.

To help develop SOFCs into a viable technology which can stretch the gap in the energy economy, research is needed to improve the reliability of the cells during manufacturing and operation. This work aims to develop the understanding of fracture mechanics of real-world structures, by understanding how temperature and partial pressure of oxygen affect the strength, fracture toughness, and flaw distributions of SOFC components. This is done by analyzing the flexural properties of bulk bars and half-cell coupons at ambient conditions and at conditions similar to those found in an SOFC. Microscopy was used to look for changes in microstructure after various treatments in addition to Weibull analysis. Additionally, thermogravimetry, conductivity, and temperature programed desorption were used to understand the atomic defect structure of a new material to relate it to the mechanical properties.

Chapter 2: Experimental Procedures

2.1 Sample Preparation

2.1.1 $SrFe_{0.2}Co_{0.4}Mo_{0.4}O_{3-\delta}$ Powder

$SrFe_{0.2}Co_{0.4}Mo_{0.4}O_{3-\delta}$ (SFCM) was created from stoichiometric amounts of strontium carbonate ($SrCO_3$, Sigma-Aldrich), iron oxide (Fe_2O_3, Sigma-Aldrich), cobalt oxide (Co_2O_3, Inframat Advanced Materials), and molybdenum oxide (MoO_3, Alfa-Aesar) using conventional solid-state methods. The constituents were ball milled for 24 hours in ethanol and dried using a $100\,°C$ oven. Afterwards the powder was calcined at $1100\,°C$ for four hours.

2.1.2 Bars

GDC bars of varying porosity were fabricated using uniaxial pressing in a rectangular die. GDC10 ($Ce_{0.9}Gd_{0.1}O_2$) powder was mixed with the desired volume of poly(methyl methacrylate) (PMMA) microspheres ($5\,\mu m$ diameter) or graphite flake to create the green body, with 0.1wt% of polyvinyl butyral added to aid in pressing and a drop of fish oil to act as a dispersant during milling. The two different pore formers were used to create differing pore geometry. The PMMA or graphite

was removed by a 400 °C pre-sintering step, and the remaining ceramic structure was sintered at 1500 °C for 4 hours. Archimedes density measurements were used to confirm porosity percent. Samples were polished with 600 grit sandpaper on all sides before testing.

Dense SFCM bars were used to maximize the total mass and mass changes during thermogravimetric testing. Samples were made by combining SFCM powder with 0.6 wt% polyethylene glycol 600, 1.8 wt% ethylene glycol, and 0.6 wt% glycerol in isopropyl alcohol and ball milling overnight. After drying at 100 °C, the powder was ground by mortar and pestle, then pressed uniaxially into rectangular bars at 30 MPa, then isostatically pressed at 30 MPa. Bars were sintered by heating to 400 °C for one hour and then 1340 °C for four hours, using a $3 °C \, min^{-1}$ heating and cooling rate. This produced bars with 97% theoretical density by Archimedes' technique.

To create fracture toughness test samples, SFCM powder was ball milled overnight with a mixture of 0.6 wt% polyethylene glycol 600, 1.8 wt% ethylene glycol, and 0.6 wt% glycerol in isopropyl alcohol. It was then dried at 100 °C, ground by mortar and pestle, pressed uniaxially into rectangular bars at 30 MPa, then isostatically pressed at 30 MPa. Sintering followed by heating to 1340 °C for four hours at 3 °C/min with a one hour hold at 400 °C to allow the binders to burn out. This process achieved dense samples at 97% average theoretical density with no apparent flaws in the bars. Bars were then cut and sanded to final dimensions of 3 mm x 4 mm x 25 mm. The chevron notch was cut using the jig described by Jenkins, Chang and Okura following the ASTM procedure. [37, 38]

2.1.3   Test Coupons

The ASL and half-cell coupons used in the flexural testing were made using tape casting. NiO and GDC powders in a 6:4 weight ratio were mixed with ethanol, toluene, and fish oil. The mixture was ball milled on a rotary mill for 24 hours. Polyvinyl butyral and benzyl butyl phthalate were added, followed by another 24 hours milling. The resulting slurry was degassed and tape cast using a 700 micron blade height. The tapes were left to dry overnight before being cut into 12 cm by 12 cm squares. Three squares were stacked and hot pressed at 49 °C and 2 tons for 30 minutes. Following this lamination, the tape was cut into rectangular coupons measuring 25mm by 10mm. The coupons were fired at 1400 °C for 4 hours. Final bar dimensions were 8.16 by 24.15 by 2.98 mm on average. For half-cell coupons GDC electrolyte slurry was prepared and tape cast with a 40 micron blade height. After the lamination of the three ASL layers, a single layer of electrolyte tape was laminated to the ASL using the same pressure for 2 hours. The sintering procedure for half-cell coupons was identical to the ASL coupons. Samples were polished with 600 grit sandpaper on edges before testing.

Tape casting was used to create test coupons of porous SFCM-GDC ASL and SFCM-GDC/GDC half-cells. Using ethanol as a solvent, SFCM-GDC was ball milled with polyvinyl butyral, benzyl butyl phthalate, 12 µm poly(methyl methacrylate) (16 wt% with respect to SFCM-GDC), and Menhaden fish oil. The tape was cast to a thickness of 110 µm on Mylar then laminated using a hot press to a final thickness of 660 µm. Dense GDC was casted to 30 µm and laminated to the top of

the SFCM-GDC to create half-cells. Individual coupons were cut from the green tape, sintered at 1200 °C for four hours, with holds at low temperatures to burn out organic binder and pore former. The final thicknesses were measured to be 400 μm for the SFCM-GDC ASL and ∼20 μm thick GDC electrolyte. Test coupons had their edges sanded to remove defects left from cutting, following ASTM standards. [39] Top and bottom surfaces were not sanded to preserve possible defects left from tape casting procedure, which would be representative of industrially manufactured SOFCs.

2.2   X-Ray Diffraction

X-ray diffraction (XRD) was used confirm phase purity of the SFCM after synthesis and during the testing process. A Bruker D8 Advance with LynxEye was used with a Cu K_α source. A step size of 0.02° was used with a dwell of 0.8 s was used. Rietveld refinement was performed on samples as synthesized, after oxidation in pure O_2 and after reduction in pure H_2 at 600 °C for both. GSAS-II was used to perform the refinement calculations and VESTA was used to visualize the unit cell. [40, 41]

2.3 Archimedes Density Measurements

2.4 Thermogravimetric Analysis

Mass of samples during oxidation and reduction cycling was measured using a Cahn D200 microbalance. The samples were placed in a crucible suspended from a platinum wire attached to the microbalance and enclosed by an alumina tube inside a furnace. Heating control was achieved with a PID loop and temperature measurement done by a K-type thermocouple placed immediately below the sample inside the alumina tube. Gas flow was controlled at a constant $50\,\mathrm{sccm}$ by mass flow controllers. 21% O_2 in dry N_2 was used for the oxidizing condition while 3% H_2 in N_2 humidified with 3% H_2O was used for the reducing conditions.

To understand the degree of reduction in test coupons, thermogravimetric analysis (TGA) was used to measure the mass loss as a function of time, temperature, and gas environment. A Cahn D200 microbalance was used to measure the weight changes as the sample was heated in a furnace with controlled atmosphere. A small section of test coupon was placed in a crucible suspended from the balance and heated to $650\,°\mathrm{C}$ at $10\,°\mathrm{C}\,\mathrm{min}^{-1}$, the environment was switched from $50\,\mathrm{sccm}$ of 21% O_2 in N_2 to $50\,\mathrm{sccm}$ of 3% H_2, 3% H_2O in N_2. Mass, temperature, and p_{O_2} measurements were taken at 30 second intervals. p_{O_2} measurements were taken using a calibrated YSZ sensor placed immediately before the sample. Samples were cooled at $10\,°\mathrm{C}\,\mathrm{min}^{-1}$ in the desired atmosphere.

Changes in mass of SFCM were measured by a Cahn D200 microbalance with

the sample suspended down a quartz tube into a furnace. The furnace used to heat the sample and quartz tube was controlled by a PID controller with a K-type thermocouple placed immediately below the sample inside the quartz tube. Gas flow was controlled at consistent 50 sccm by mass flow controllers, which mixed dry nitrogen, oxygen, hydrogen, and humidified nitrogen to obtain the p_{O_2} desired. Measurements of the p_{O_2} were taken by a calibrated YSZ oxygen sensor at 800 °C located before the sample. Again, intermediate p_{O_2} ranges were not able to be tested due to SFCM's incompatibility with the species required to create that environment.

Further details of the operation of the TGA and its various components are given in Appendix B.

To prepare the sample, it was pre-weighed, wrapped in platinum wire and suspended from the balance, placed in the furnace with simulated air (21% O_2, 79% N_2) flowing. Once the mass had stabilized, the furnace was heated to 800 °C to allow for any organic contamination to burn off. After the mass stabilized at this elevated temperature the sample was introduced to various environments. The mass of the sample would be noted only after steady state had been reached for a condition. After testing a sample, a bar of alumina was cut to the same dimensions as the sample and the process was repeated to obtain a blank which could be subtracted from the measurements to remove buoyancy effects.

Oxygen non-stoichiometry was calculated using Equation 2.1, where $\Delta\delta$ is the change in oxygen stoichiometry, MW_{SFCM} is the molecular weight of SFCM (208.74 g mol^{-1}), MW_O is the molecular weight of oxygen (16.0 g mol^{-1}), w_{sample} is the weight of the sample, and Δw is the weight change as recorded by the TGA. The

16

oxygen vacancy concentration ($[V_O^{\bullet\bullet}]$) is calculated using Equation 2.2, where ρ is the density of SFCM and N_A is Avogadro's number. To calculate the oxygen vacancy concentration, the non-stoichiometry of SFCM at a point needs to be established. For this work, based on the plateau present in the data at oxidizing conditions, it is assumed that in a pure oxygen environment ($log(p_{O_2}) = 0$) all oxygen vacancies are filled with no oxygen interstitial or surface species, thus $\delta = 0$.

$$\Delta\delta = \frac{MW_{SFCM}}{MW_O \; w_{sample}}\Delta w \tag{2.1}$$

$$[V_O^{\bullet\bullet}] = \frac{\delta\rho N_A}{MW_{SFCM}} \tag{2.2}$$

2.4.1   Temperature Programed Desorption

The effluent from the TGA was used as the inlet to a mass spectrometer (MS) to perform temperature programmed desorption. The sample was prepared as before and heat treated to remove any carbon contaminants but was allowed to cool under simulated air. It was then heated to $800\,^{\circ}\mathrm{C}$ at $5\,^{\circ}\mathrm{C\,min^{-1}}$ under a $50\,\mathrm{sccm}$ flow of nitrogen as the MS measured the $32\,\mathrm{m/z}$ signal which corresponded to O_2 desorption. Additional m/z signals were monitored to observed for other species.

2.5   Conductivity

Electric conductivity across p_{O_2} was measured using the four-wire technique and a Stanford SR 830 lock-in amplifier. A bar shape sample was used with dimensions of $6.46\,\mathrm{mm} \times 3.3\,\mathrm{mm} \times 1.3\,\mathrm{mm}$. Gold paste was used as a current collector, and the current range was between 0.005 to $0.05\,\mathrm{A}$. A yttria-stabilized zirconia (YSZ)

oxygen sensor operating at $800\,^\circ$C was used to monitor the changes in oxygen partial pressures. Intermediate p_{O_2} ranges were not tested due to an incompatibility between SFCM and the CO and CO_2 required to obtain those p_{O_2}.

Conductivity during redox cycling was measured using rectangular bars of SFCM and SFCM-GDC (2:1) composite. The samples were connected to a Keithley 2400 source meter by silver paste and wire. Using an in-house built reactor, the sample could be heated and the gas environment could be controlled. An initial measurement was taken after heating and 50 hours of exposure to 10% H_2 in N_2, then the sample exposed cycled between air and reducing conditions over a period of 14 days.

2.6   Mechanical Testing

Measurements of mechanical properties were collected using a Tinius Olsen 10ST Universal Testing Machine equipped with a $250\,$N load cell. Experiments where any samples would be tested at elevated temperatures or under reducing environments were conducted using a custom built three point flexural test fixture placed inside a gas-tight chamber and furnace. Otherwise, a fully-articulating four point flexural test fixture was used. Samples tested at ambient conditions were placed on the appropriate testing fixture and loaded until failure. For samples tested at elevated temperatures the sample was heated in the test chamber at $10\,^\circ\text{C}\,\text{min}^{-1}$, allowed to equilibrate for 20 minutes, then tested. Samples to be reduced were placed in the chamber, heated and exposed to reducing gas for 18 hours before being tested.

All tests conducted in the UTM (Tinius Olsen 10ST with 250 N load cell) were done at a rate of $0.2\,\mathrm{mm\,min^{-1}}$ with a 20 mm lower span. After measuring the force at fracture, stress was calculated using Equation 3.1 for 3-point flexural of rectangular samples, where σ_f is the stress at failure, F is the load at failure, L is the span of the fixture, b is the width of the sample and d is the thickness of the sample. At room temperature, the coupons or bars were loaded into the fixture and tested in batches of 5 per condition. Occasionally samples would break or be damaged before testing, reducing the sample set. For sample sets at elevated temperatures in ambient atmosphere, the samples were loaded into the front of the chamber, acting as a staging area, prior to heating the on fixture in the center. Upon transferring the next coupon from the staging area to the fixture, a 20 minute waiting period was used to ensure that the coupon had reached thermal equilibrium prior to testing.

$$\sigma_f = \frac{3FL}{2bd^2} \qquad (2.3)$$

Following the completion of the set, all coupon pieces were cooled at a rate of $10\,^{\circ}\mathrm{C/min}$. For testing in reducing atmosphere, each coupon was reduced and tested individually. Half-cell coupons were tested in two orientations, "electrolyte-up" and "electrolyte-down." These orientations cause the dense electrolyte layer to experience compressive or tensile stress. The "electrolyte-up" orientation subjects the electrolyte to compressive stress and vice-versa.

Following the destructive tests, SEM analyses of the fracture surfaces were performed. The purpose of this was to observe the trans-granular, inter-granular, or mixed nature of crack propagation, and to find any anomalous features on the

Figure 2.1: Assembled Alumina 3-Point Bend Fixture

fracture surface, as well as to observe pore geometry.

2.6.1 Development of Mechanical Test Apparatus

To develop a testing apparatus capable of simulating the various conditions experienced by operating SOFCs, appropriate materials were chosen based on thermal and chemical stability criteria. Alumina was chosen to build the bend fixture due to its chemical stability and high hardness. The sample rests crossways on two stationary 6.35 mm diameter rods which are placed in troughs separated by 20 mm. The upper half of the fixture consists of a 6.35 mm rod used to apply stress to the sample from the UTM crosshead. Both pieces are attached using silica-based cement to 300 mm rods attached at the anchor points of the UTM. Assembly and alignment is assisted with the use of a 3D printed jig to ensure repeatability. The complete alumina, 3-point bend fixture is seen in Figure 3.1 with the two bottom rollers, a sample, and the top roller making contact, applying flexural stresses to the sample.

To create the atmosphere control system, a combination of standard and custom vacuum system parts were used to enclose the bend fixture. For the main body of the chamber, a 3-inch inner diameter, stainless steel tee was made with QF80 and QF50 flanges. Welded NPT ports on top and bottom allow for gas inlet and
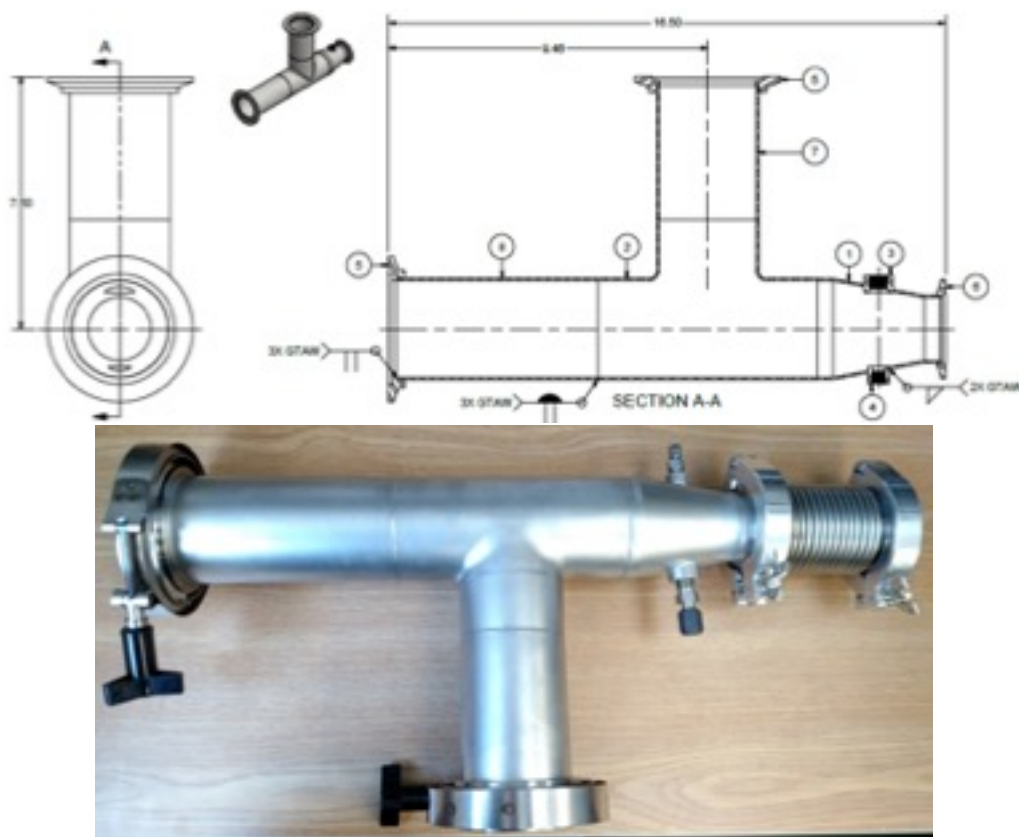
Figure 2.2: Design drawing and photo of mechanical testing atmospheric chamber

outlet and the introduction of a thermocouple through a Swagelok Ultra-Torr fitting. Figure 3.2 shows the engineering drawings and photo of the custom pieces from A&N Corp. Flexible bellows allow for the motion of the cross-bar to be translated into the fixture, requiring the subtraction of the spring force to be removed during analysis. The alumina fixture was then inserted through each end and the chamber incorporated into the furnace with QF50 to 1/2 inch tube adapters that fit over the alumina rods.

To heat the fixture and chamber, a 1 ft. cube was assembled from steel plates with cutouts on top, bottom and front. Steel wire mesh was used to create

a framework inside to hold nickel-chromium alloy heating elements. Silica-based wool insulation was packed between the center cavity and the case walls. A K-type thermocouple was inserted into the chamber and used with an external PID controller to cycle the heating elements. The furnace was placed on a supporting scaffold to hold it in position during tests. The test fixture, atmosphere chamber, and furnace were affixed together as one unit and inserted into the UTM. The design was compared and qualified to a regular steel 3-point bend apparatus to ensure accurate results at room temperature.

2.6.2   Atmospheric Treatment

To test individual coupons under reducing environments, samples were loaded into the test chamber at $400\,°C$, after previous pre-heating in the staging area. After 20 minutes, the temperature would be increased to the desired set-point of $650\,°C$ at a ramp rate of $10\,°C\,min^{-1}$ and the gas would be switched first to N_2 to flush the chamber, then to humidified argon containing 3% H_2. It would then be allowed to sit for 18 hours before testing to allow reduction. After testing, the chamber would be flushed again with N_2 and cooled to $400\,°C$ before opening to change samples and repeat the process.

If samples had been previously reduced as a batch by exposure to hydrogen in a tube furnace and cooled under hydrogen, the atmospheric treatment was shortened, as supported by TGA results. Pre-reduced samples were loaded into the chamber at or below $400\,°C$, the chamber flushed N_2, then with H_2 in Ar. After this the chamber

would be heated to $650\,°C$, the sample tested after a 30 minute period, and cooled

back down to $400\,°C$. At this point, the chamber would be flushed with N_2. While

the chamber maintained a positive pressure of N_2, it could be opened, a new sample

loaded, closed, and allowed to flush. This procedure allows for the batch reduction

of many test coupons and replaced the 18 hour reduction time with a shorter 30

minute period.

2.6.3   Fracture Strength

A loading rate of $0.2\,mm/min$ was used for all strength measurements. Strength

was calculated from the maximum force measured before failure according to Equation

2.4 or 3.1 depending on if the four point or three point fixture is used respectively,

where σ is the strength, P is the maximum force, L is the span width of the test

fixture, b is the width of the sample and d is the thickness of the sample. Equation

2.4 is for a fixture where the top span is $1/2$ the width of the bottom span. [39]

$$\sigma = \frac{3PL}{4bd^2} \tag{2.4}$$

2.6.4   Fracture Toughness

The fracture toughness of chevron notched samples were measured using a

loading rate of $0.001\,mm/min$. Fracture toughness was calculated from the maximum

force using Equation 2.5 or 2.6 for four point or three point fixtures. [38, 42] Y^*_{min} is

the shape factor as calculated by Equation 2.7, S_o and S_i are the outer and inner

spans, B is the width of the sample, W is the height of the sample, a_0 is the distance

from the tip of the chevron notch to the bottom of the sample, and a_1 is the average distance from the side of the chevron notch to the bottom of the sample. Each sample was measured after failure, but in this study the approximate values were $S_o = 40mm$, $S_i = 20mm$, $B = 3.0mm$, $W = 4.0mm$, $a_0 = 0.80mm$, $a_1 = 3.8mm$. Fracture toughness was measured only under air at room temperature and up to $600\,°C$. Under reduction the fracture toughness bars would spontaneously fracture, preventing measurements under that condition.

$$K_{Ivb} = Y^*_{min} \left[\frac{P[S_o - S_i]}{BW^{3/2}} \right] 10^{-6} \tag{2.5}$$

$$K_{Ivb} = Y^*_{min} \left[\frac{P}{BW^{1/2}} \right] 10^{-6} \tag{2.6}$$

$$Y^*_{min} = \frac{0.38742 - 3.0919(a_0/W) + 4.2017(a_1/W) - 2.3127(a_1/W)^2 + 0.6379(a_1/W)^3}{1.0000 - 2.9686(a_0/W) + 3.5056(a_0/W)^2 - 2.1374(a_0/W)^3 + 0.0130(a_1/W)} \tag{2.7}$$

2.7   Scanning Electron Microscopy

Chapter 3: High Temperature Mechanical Behavior of Porous Ceria and Ceria-Based SOFCs

3.1 Introduction

For planar SOFCs, a standard stack design consists of a number of square cells separated by metal interconnects. [43] These interconnects act as current collectors, gas channels, and separators to prevent fuel and air from mixing. Sealing of these stacks is accomplished by compressing the layered structure which includes sealing material. As more compressive force is applied to the stack, the quality of the seals improves. However, any cell which is not perfectly flat will experience flexural stress as a result and this can lead to cells fracturing. Due to the brittle nature of the ceramic materials that constitute SOFCs, a very thorough understanding of the mechanical limits of these devices is critical to their successful deployment.

The vulnerability of SOFCs to mechanical failure is a well-known issue. However, much of the research into this phenomenon has focused on yttrium stabilized zirconia (YSZ) based devices. [21,44,45] This material has been the standard for the field and has desirable mechanical properties but requires high temperatures to function well. As efforts are made to lower SOFC operating temperatures, a shift to ceria-based

electrolytes has occurred. Less attention has been given to the mechanical behavior of doped ceria materials across SOFC operating conditions.

Much of the study of fracture in ceramic materials has been done on technical ceramics for medical applications and for coating metal components. [46–53] These materials are optimized for fracture toughness and durability and very rarely experience temperatures above a few hundred degrees Celsius. The fracture surface analysis and correlations between microstructure and strength described for these materials are a valuable starting point for investigating fuel cell materials. However, there is a lack of extensive investigation into the properties of IT-SOFC materials at their expected operating temperatures and environments.

Efforts have been made to comprehensively examine the mechanical properties of SOFC materials and the effect of non-standard conditions on those properties. Nakajo et al. conducted a wide ranging study of materials used in anode supported SOFCs which included some attention to temperature and atmosphere effects. [45] While providing a solid base of material knowledge, this work did not fully cover materials beyond YSZ and there remains a need for further testing, especially for doped ceria. Flexural strength and Young's modulus measurements for gadolinium doped ceria (GDC) have been carried out in ambient conditions by Yasuda et al. [54] They characterized the effects of sintering temperature on density and the resulting mechanical properties. Further testing of this material system at elevated temperatures and anode gas reducing environments must be done to fully understand the mechanical behavior of GDC.

This article presents the results of a broad range of flexural tests involving the

materials used in ceria-based anode supported SOFCs along with the assembled half-cells. Using a purpose-built temperature controlled environmental chamber installed in a universal testing machine (UTM), porous doped ceria bars, anode support layers (ASL) composed of nickel and doped ceria cermet, and half-cells composed of an ASL and a doped ceria electrolyte were tested. The various test conditions used included expected operating temperatures (450 °C–650 °C), and both reducing and oxygenated atmospheres. These variations in test conditions are important because these cells must maintain their integrity from when they are first placed in a sealed stack to when they reach operating conditions. In particular, this study was intended to determine at what point in their life SOFCs are most vulnerable to mechanical failure and the mechanisms involved. Additionally, the effect of the anode-electrolyte interface on flexural strength was explored.

3.2   Experimental

3.2.1   Sample Preparation

GDC bars of varying porosity were fabricated using uniaxial pressing in a rectangular die. GDC10 ($Ce_{0.9}Gd_{0.1}O_2$) powder was mixed with the desired volume of poly(methyl methacrylate) (PMMA) microspheres (5 µm diameter) or graphite flake to create the green body, with 0.1wt% of polyvinyl butyral added to aid in pressing and a drop of fish oil to act as a dispersant during milling. The two different pore formers were used to create differing pore geometry. The PMMA or graphite was removed by a 400 °C pre-sintering step, and the remaining ceramic structure

27

was sintered at 1500 °C for 4 hours. Archimedes density measurements were used to confirm porosity percent. Samples were polished with 600 grit sandpaper on all sides before testing.

The ASL and half-cell coupons used in the flexural testing were made using tape casting. NiO and GDC powders in a 6:4 weight ratio were mixed with ethanol, toluene, and fish oil. The mixture was ball milled on a rotary mill for 24 hours. Polyvinyl butyral and benzyl butyl phthalate were added, followed by another 24 hours milling. The resulting slurry was degassed and tape cast using a 700 micron blade height. The tapes were left to dry overnight before being cut into 12 cm by 12 cm squares. Three squares were stacked and hot pressed at 49 °C and 2 tons for 30 minutes. Following this lamination, the tape was cut into rectangular coupons measuring 25mm by 10mm. The coupons were fired at 1400 °C for 4 hours. Final bar dimensions were 8.16 by 24.15 by 2.98 mm on average. For half-cell coupons GDC electrolyte slurry was prepared and tape cast with a 40 micron blade height. After the lamination of the three ASL layers, a single layer of electrolyte tape was laminated to the ASL using the same pressure for 2 hours. The sintering procedure for half-cell coupons was identical to the ASL coupons. Samples were polished with 600 grit sandpaper on edges before testing.

3.2.2 Thermogravimetric Analysis

To understand the degree of reduction in test coupons, thermogravimetric analysis (TGA) was used to measure the mass loss as a function of time, temperature,

and gas environment. A Cahn D200 microbalance was used to measure the weight changes as the sample was heated in a furnace with controlled atmosphere. A small section of test coupon was placed in a crucible suspended from the balance and heated to $650\,°C$ at $10\,°C\,min^{-1}$, the environment was switched from $50\,sccm$ of 21% O_2 in N_2 to $50\,sccm$ of 3% H_2, 3% H_2O in N_2. Mass, temperature, and p_{O_2} measurements were taken at 30 second intervals. p_{O_2} measurements were taken using a calibrated YSZ sensor placed immediately before the sample. Samples were cooled at $10\,°C\,min^{-1}$ in the desired atmosphere.

3.2.3   Development of Mechanical Test Apparatus

To develop a testing apparatus capable of simulating the various conditions experienced by operating SOFCs, appropriate materials were chosen based on thermal and chemical stability criteria. Alumina was chosen to build the bend fixture due to its chemical stability and high hardness. The sample rests crossways on two stationary $6.35\,mm$ diameter rods which are placed in troughs separated by $20\,mm$. The upper half of the fixture consists of a $6.35\,mm$ rod used to apply stress to the sample from the UTM crosshead. Both pieces are attached using silica-based cement to $300\,mm$ rods attached at the anchor points of the UTM. Assembly and alignment is assisted with the use of a 3D printed jig to ensure repeatability. The complete alumina, 3-point bend fixture is seen in Figure 3.1 with the two bottom rollers, a sample, and the top roller making contact, applying flexural stresses to the sample.

To create the atmosphere control system, a combination of standard and custom

Figure 3.1: Assembled Alumina 3-Point Bend Fixture

vacuum system parts were used to enclose the bend fixture. For the main body of the chamber, a 3-inch inner diameter, stainless steel tee was made with QF80 and QF50 flanges. Welded NPT ports on top and bottom allow for gas inlet and outlet and the introduction of a thermocouple through a Swagelok Ultra-Torr fitting. Figure 3.2 shows the engineering drawings and photo of the custom pieces from A&N Corp. Flexible bellows allow for the motion of the cross-bar to be translated into the fixture, requiring the subtraction of the spring force to be removed during analysis. The alumina fixture was then inserted through each end and the chamber incorporated into the furnace with QF50 to 1/2 inch tube adapters that fit over the alumina rods.

To heat the fixture and chamber, a 1 ft. cube was assembled from steel plates with cutouts on top, bottom and front. Steel wire mesh was used to create a framework inside to hold nickel-chromium alloy heating elements. Silica-based wool insulation was packed between the center cavity and the case walls. A K-type thermocouple was inserted into the chamber and used with an external PID controller to cycle the heating elements. The furnace was placed on a supporting scaffold to hold it in position during tests. The test fixture, atmosphere chamber, and furnace were affixed together as one unit and inserted into the UTM. The design was

Figure 3.2: Design drawing and photo of mechanical testing atmospheric chamber

compared and qualified to a regular steel 3-point bend apparatus to ensure accurate results at room temperature.

3.2.4 Bend Testing

All tests conducted in the UTM (Tinius Olsen 10ST with 250 N load cell) were done at a rate of $0.2\,\mathrm{mm\,min^{-1}}$ with a 20 mm lower span. After measuring the force at fracture, stress was calculated using Equation 3.1 for 3-point flexural of rectangular samples, where σ_f is the stress at failure, F is the load at failure, L is the span of the fixture, b is the width of the sample and d is the thickness of the sample. At room temperature, the coupons or bars were loaded into the fixture and tested in batches of 5 per condition. Occasionally samples would break or be damaged before testing, reducing the sample set. For sample sets at elevated temperatures in ambient atmosphere, the samples were loaded into the front of the chamber, acting as a staging area, prior to heating the on fixture in the center. Upon transferring the next coupon from the staging area to the fixture, a 20 minute waiting period was used to ensure that the coupon had reached thermal equilibrium prior to testing.

$$\sigma_f = \frac{3FL}{2bd^2} \qquad\qquad (3.1)$$

Following the completion of the set, all coupon pieces were cooled at a rate of $10\,°\mathrm{C/min}$. For testing in reducing atmosphere, each coupon was reduced and tested individually. Half-cell coupons were tested in two orientations, "electrolyte-up" and "electrolyte-down." These orientations cause the dense electrolyte layer to experience compressive or tensile stress. The "electrolyte-up" orientation subjects the electrolyte

to compressive stress and vice-versa.

Following the destructive tests, SEM analyses of the fracture surfaces were performed. The purpose of this was to observe the trans-granular, inter-granular, or mixed nature of crack propagation, and to find any anomalous features on the fracture surface, as well as to observe pore geometry.

3.2.5   Atmospheric Treatment

To test individual coupons under reducing environments, samples were loaded into the test chamber at 400 °C, after previous pre-heating in the staging area. After 20 minutes, the temperature would be increased to the desired set-point of 650 °C at a ramp rate of $10\,°C\,min^{-1}$ and the gas would be switched first to N_2 to flush the chamber, then to humidified argon containing 3% H_2. It would then be allowed to sit for 18 hours before testing to allow reduction. After testing, the chamber would be flushed again with N_2 and cooled to 400 °C before opening to change samples and repeat the process.

If samples had been previously reduced as a batch by exposure to hydrogen in a tube furnace and cooled under hydrogen, the atmospheric treatment was shortened, as supported by TGA results. Pre-reduced samples were loaded into the chamber at or below 400 °C, the chamber flushed N_2, then with H_2 in Ar. After this the chamber would be heated to 650 °C, the sample tested after a 30 minute period, and cooled back down to 400 °C. At this point, the chamber would be flushed with N_2. While the chamber maintained a positive pressure of N_2, it could be opened, a new sample

loaded, closed, and allowed to flush. This procedure allows for the batch reduction of many test coupons and replaced the 18 hour reduction time with a shorter 30 minute period.

3.3   Results

3.3.1   Porosity and Pore Former Choice

As expected, GDC bars with greater porosity displayed lower flexural strength values as compared to less porous samples. The relationship between porosity and strength followed an exponential trend. This behavior is well established for porous ceramics and is described by Equation 3.2, where σ_f is the flexural strength with porosity, σ_o is the flexural strength without porosity, η is a geometric constant dependent on the system, and P is the volume percent porosity of the sample. [55]

$$\sigma_f = \sigma_o e^{-\eta P} \tag{3.2}$$

The data was fit using this equation and both a fixed geometric constant, η, of 0.047 (Figure 3.3a) and a variable geometric constant (Figure 3.3b).

Chi-squared values, indicating the divergence of the fit from the measured data for each sample set, were calculated for the two fitting methods and are displayed in Table 3.1.

The deviance from the fit curve for the fixed η method is quite large relative to the variable η fit for both sample sets tested at 650 °C. Both fitting methods are fairly poor in the case of the room temperature graphite set. The poor fitting
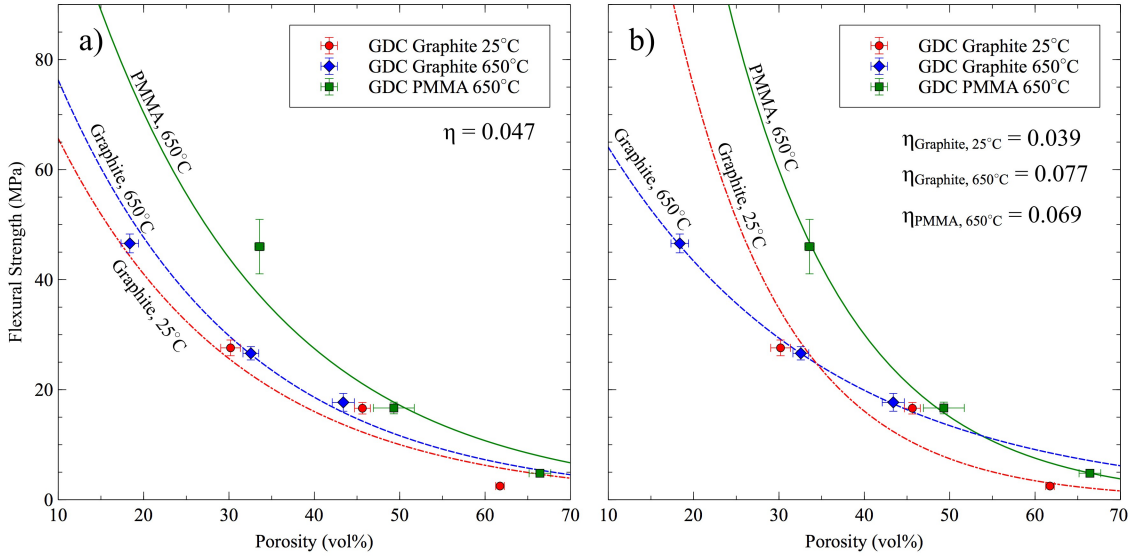
Figure 3.3: Flexural strength-porosity dependence for porous GDC10 at 650 °C and 25 °C using spherical PMMA or graphite flake pore former: a) Measured strengths fitted using fixed geometric constant; b) Measured strengths fitted using different geometric constants

Table 3.1: Chi-squared values for fixed η and variable η fits of porous GDC strength data (Figure 3.3

Sample Set	χ^2	χ^2
	(Fixed η)	(Variable η)
GDC PMMA 650 °C	3.406	0.062
GDC Graphite 650 °C	0.668	0.008
GDC Graphite 25 °C	3.575	5.063

results in this case is due to the >60% porosity samples. The flatter pore geometry caused by the graphite likely leads to comparatively greater strength loss at high porosity due to likely greater pore connectivity. The comparison between the high temperature data sets is the most useful, given this, and the fact that SOFCs operate at this temperature. The poor fit of fixed η models suggests that a material-specific η value may be an oversimplification of the porosity-stress relationship in ceramics.

Samples tested at higher temperatures displayed a slightly higher flexural strength. Generally, it is expected that increasing temperature lowers strength of dense ceramics once plastic deformation processes become activated at high temperatures. [56] Below the temperature at which plastic deformation starts to occur, temperature has a minimal effect on flexural strength of dense ceramics. For dense GDC it has been demonstrated that the strength decreases by 19% between room temperature and 800 °C. [12] Porosity changes this behavior, by essentially creating a composite material, keeping the rate of change constant or increasing with temperature. [57] For porous GDC, thermal expansion places a compressive stress on any surface flaws that are sites for crack initiation and propagation. Additionally, the porosity helps reduce bulk stresses caused by thermal expansion. These two effects increase the material's fracture strength more than any decrease from plastic deformation at 625 °C.

Cross-sectional SEM of the fracture surfaces of the porous GDC samples, both PMMA and graphite, is shown in Figure 3.4. Figure 3.4a shows individual spherical pores left by the PMMA while Figure 3.4b has an inter-connected network of long pores left by the graphite flakes.
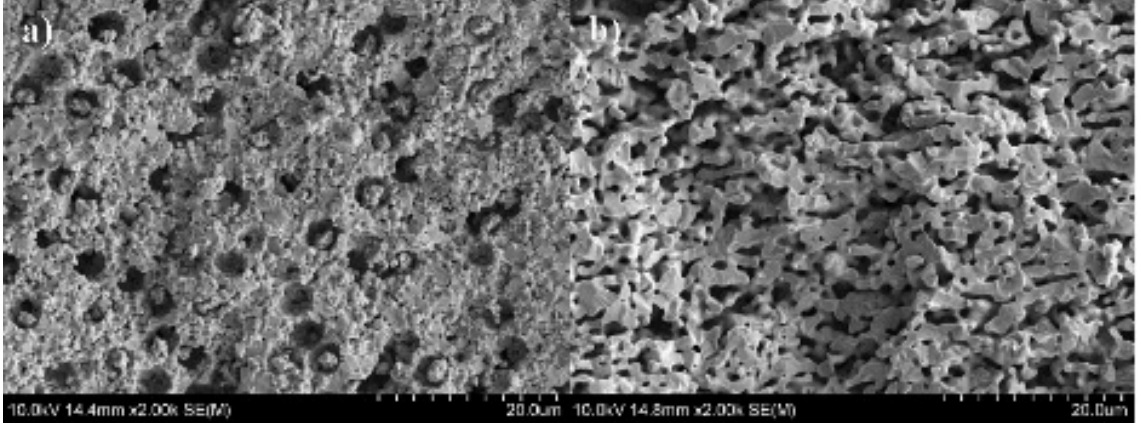
Figure 3.4: SEM micrographs of porous GDC bars made using: a) PMMA
pore former; b) graphite flake pore former

The differences in quality of fit between Figure 3.3a and Figure 3.3b shows that
the geometric factor is microstructurally dependent. Samples with porosity formed
using PMMA spheres showed significantly greater strength as compared to samples
with graphite-formed porosity. This can be explained by the effect of pore geometry
on crack initiation and propagation in the ceramic. If a crack enters a pore, the pore
can now be considered the new crack tip. The energy required to advance the crack
is highly dependent on the geometry of the tip. For a spherical pore, this geometric
factor is maximized and results in higher resilience to fracture. This is summarized
by Equation 3.3 where σ_o is the stress at the crack tip, c is the length of the crack
tip and ρ is the radius of curvature of the crack tip. [58]

$$\sigma_f = \frac{\sigma_o}{2}\sqrt{\frac{\rho}{c}} \tag{3.3}$$

Based on the mechanical behavior of these samples, porous ceramics should
be designed and constructed such that the pore geometry is as low aspect ratio as
possible to maximize strength.

3.3.2 Flexural Stress Orientation

Figure 3.5 shows the measure flexural strengths of a number of SOFC coupon samples. Anode support coupons were tested along with half-cells consisting of anode supports and electrolyte layers at temperatures ranging from 25 °C to 650 °C. The highest temperature test was repeated with coupons under reducing conditions (3% H_2, balance Ar).

All unreduced sample types showed increased strength at elevated temperatures with little difference between types at a given temperature. The high-temperature reduced coupons displayed large differences in strength depending on the orientation of the sample. Tests in which the dense electrolyte layer was placed in compression resulted in the highest strength values, while the samples were weakest when the electrolyte was placed in tension. In reduced samples, the anode support layer becomes a ceramic-metal composite and is therefore somewhat elastic while the electrolyte remains a brittle ceramic. The electrolyte-in-compression condition maximizes the mechanical performance of the coupon by placing the layers in their preferred stress state.

Figure 3.6 shows the box plots for the unreduced SOFC coupon samples. A Student's t-test was used to statically determine if the means of samples tested at different conditions were equal based on 95% confidence. There is no discernible difference in the strength between the three sample types at each temperature. At elevated temperature there was a significant difference in the modulus of ASL only samples and samples with electrolyte in tension with a p-value of 0.0091. This
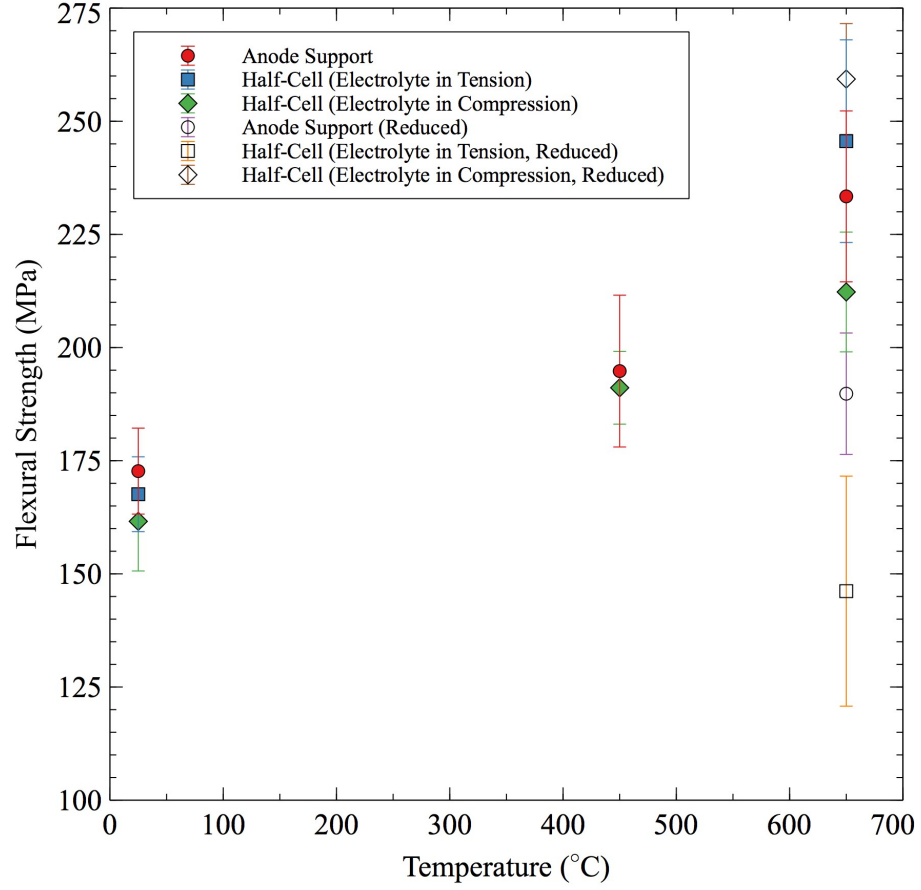
Figure 3.5: Temperature dependent strength of Ni-GDC anode supports and half-cells in both air (filled data points), and reducing atmosphere (3% H$_2$, balance Ar, hollow data points), tested in both "electrolyte-up" and "electrolyte-down" orientations resulting in the electrolyte layer experiencing tension and compression, respectively
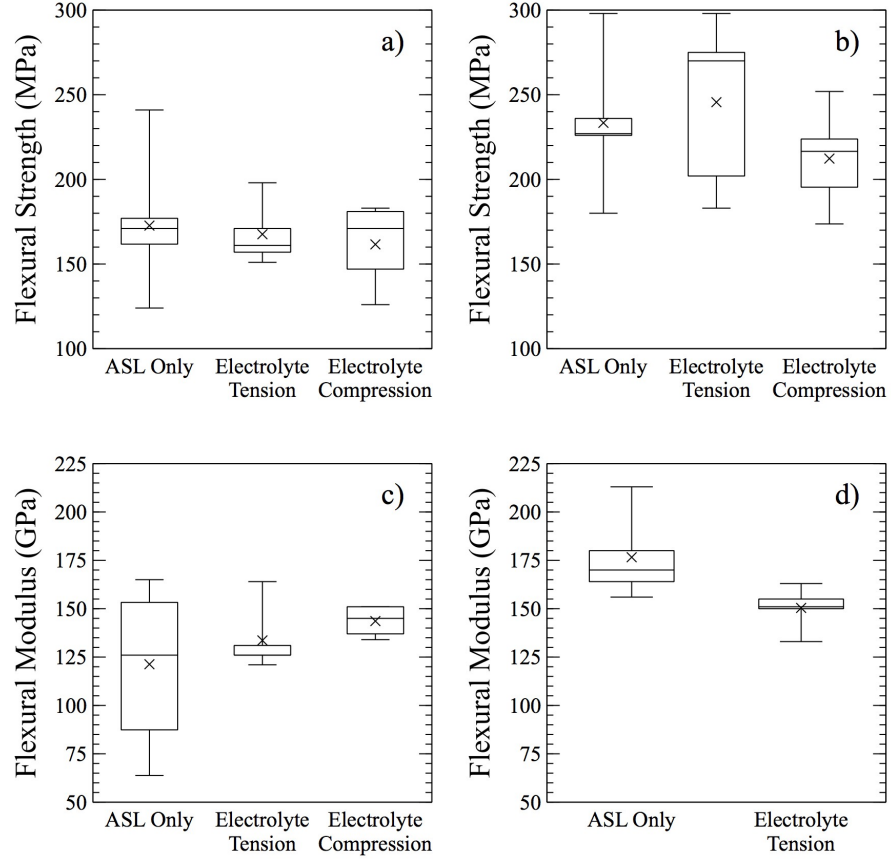
Figure 3.6: Flexural test measurements of coupons sample sets: a) Strength at 25 °C b) Strength at 650 °C c) Modulus at 25 °C d) Modulus at 650 °C

difference was not present at room temperature. As the materials reach elevated temperature, small differences in elasticity become magnified due to different thermal effects on dense and porous layers.

Additionally, SEM analysis of the fractured half-cells showed very good adhesion between layers (Figure 3.7). Delamination is a common failure mode in layered ceramics and one that would be particularly damaging to SOFCs due to resulting ionic conductivity loss between layers. [59] In the half-cell coupons, it was clear that
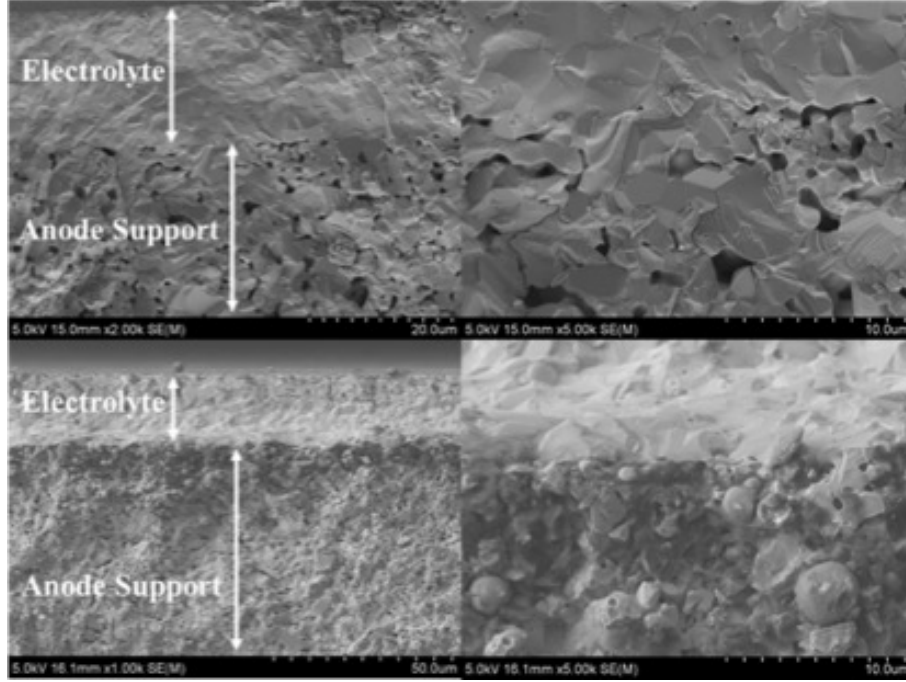
Figure 3.7: SEM micrographs of unreduced and reduced half-cell fracture surface: tested in air at 25 °C (top) and tested in reducing atmosphere at 650 °C (bottom), showing good adhesion between anode and electrolyte

the fracture plane contained mixed transgranular and intergranular fracture. Some grains were sheared through while others remained whole. The striations visible in Figure 3.7 are characteristic of fracture proceeding through a grain, while other grains remained whole.

3.3.3   Reduction and Strength

Mass loss of SOFC half-cell coupons exposed to reducing atmosphere at various elevated temperatures is shown in Figure 3.8. Mass loss is attributed to the reduction of NiO, used as a precursor in fabrication, to Ni metal, which serves as the catalyst for fuel oxidation and electronic conductor, and the reduction of ceria to $CeO_{2-\delta}$.

Table 3.2: Summary of fit parameters for reduction of NiO-GDC/GDC half-cell coupons under 3% H_2, 3% H_2O, 94% N_2 at different temperatures.

Temperature (°C)	Exponential Rate (h^{-1})	Asymptote (Mass %)
550	0.0463	89.78
575	0.135	89.09
600	0.182	88.36
650	0.512	87.75
750	0.821	87.87

Ni-GDC/GDC half cells showed the expected trend of increasing reduction rate at higher temperatures. Reduction curves were fit to an exponential decay and the summary of parameters is shown in Table 3.2. At 650 °C and 700 °C the reduction occurs very quickly, reaching steady state values after 18 hours. 550 °C showed a much slower mass loss than even 575 °C. At temperatures lower than 550 °C the kinetics are slow enough to tolerate a brief exposure to oxygen without re-oxidizing the sample. Of note in the reduction is that each temperature appears to approach a different asymptote, showing that the amount of NiO and GDC reduced at steady state is dependent on the temperature of the cell. This will affect the mechanical properties of the cells as it changes both the porosity and amount of nickel metal in the samples.

Ni-GDC/GDC fuel cells are sensitive to re-oxidation once reduced. Re-oxidation causes fracture of cells due to the large volume difference between NiO and Ni. [45]
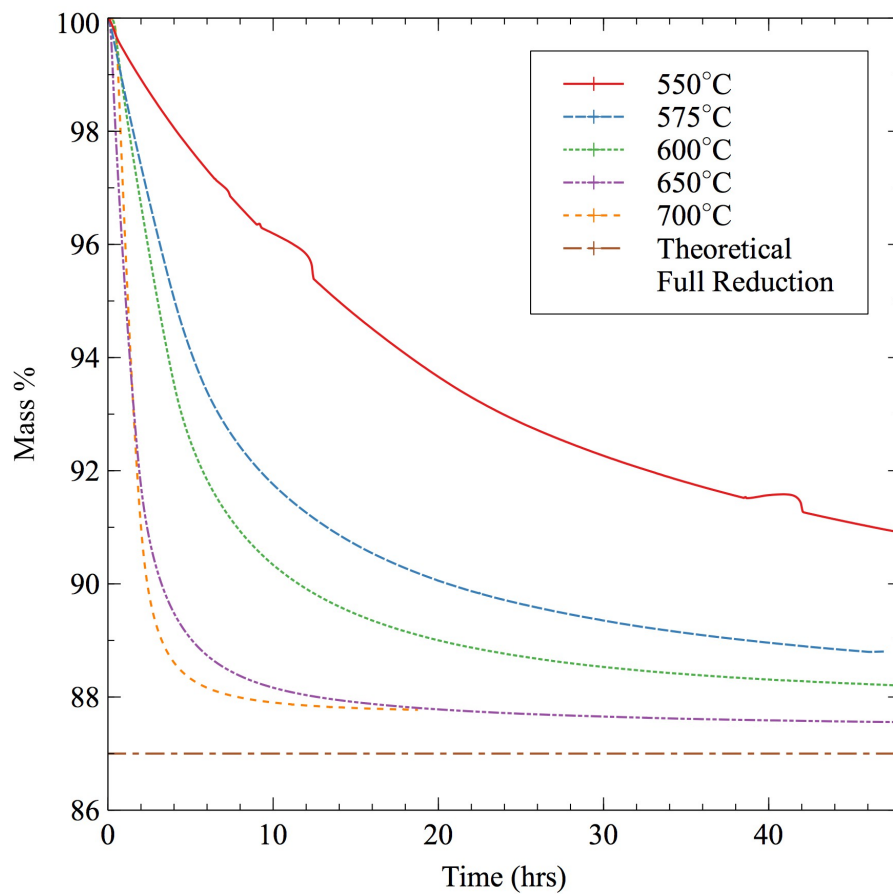
Figure 3.8: Thermogravimetric analysis curves for Ni-GDC/GDC half-cells showing mass loss over time at temperatures ranging from $550\,°C$ to $750\,°C$ in 3% H_2 3% H_2O balance N_2, $50\,sccm$ flow.

Based on the results from the TGA, the reaction rates below 300 °C are sufficiently slow to allow for the exposure of a reduced cell to oxygen without detrimental results. [60] To confirm this a sample was measured by TGA to ensure no mass gain during oxygen exposure and the strength of samples were tested to ensure there was no discernible difference between reduction methods.

For TGA analysis, a piece of a half cell was heated to 650 °C with a $10 \, °\text{C} \, \text{min}^{-1}$ ramp rate and reduced. It was then cooled while still under reducing atmospheres. Once below 100 °C, it was exposed to simulated air (21% O_2) for 18 hours, placed back into reducing atmosphere, and heated back up to 650 °C. Figure 3.9 shows the change in mass overlaid onto the temperature and oxygen partial pressure experienced by the sample. Following this treatment, the cell showed no mass gain during the oxygen exposure and continued to reduce at the same rate as before once it was returned to the initial conditions. This shows that cells which are cooled appropriately do not re-oxidize and could be handled in between a batch reduction of cells, and their assembly into a stack configuration.

Box plots of flexural strength and modulus of the in-situ reduced and batch reduced coupons are shown in Figure 3.10. Mechanical strength of half-cell coupons which had been reduced in-situ with an 18 hour reduction time showed no difference in strength when compared with coupons which had been previously batch reduced, cooled, and reheated under reducing environments. Both of these sample types showed a dramatic decrease in strength and Young's modulus compared to the un-reduced samples, but no statistically significant difference between treatments. The decrease in strength and modulus is due to the increase in porosity and conversion of
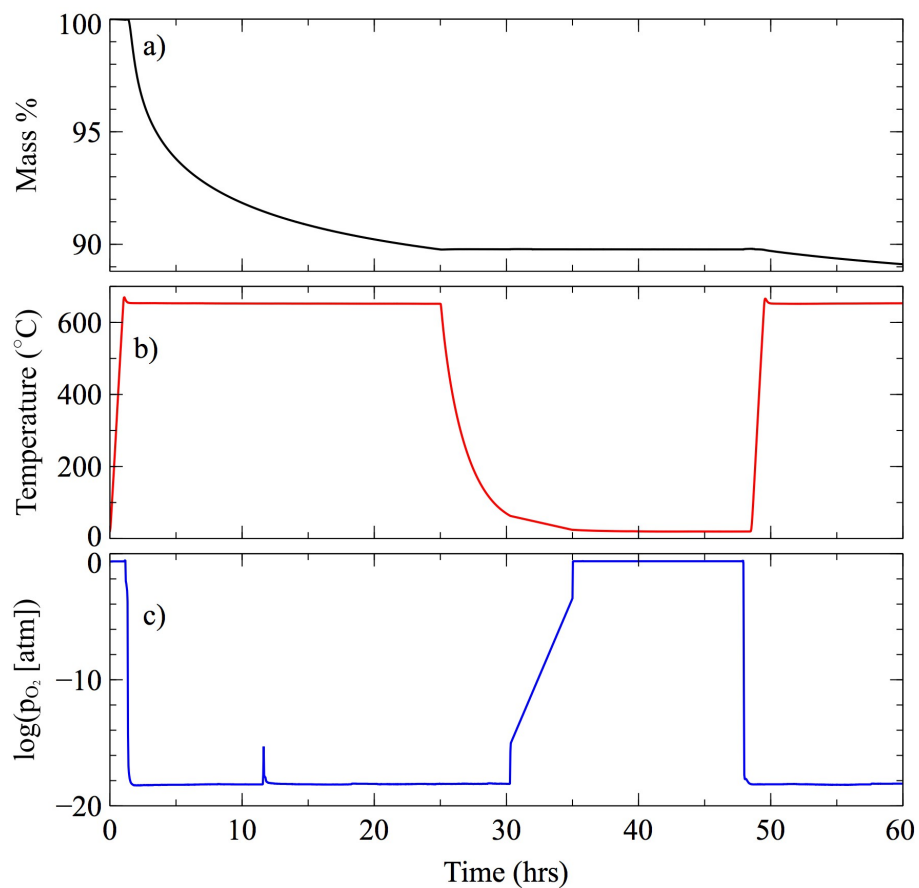
Figure 3.9: Thermogravimetric analysis of Ni-GDC/GDC half-cell showing no mass gain after reduction and exposure to room temperature and simulated air: a) Mass loss of interrupted reduction with exposure to ambient condition; b) Temperature of sample during cycle c) Oxygen partial pressure measured at the sample during cycle

NiO to metallic nickel in the cells. The decrease in variation between measurements in reduced cells is likely due to the increased number of large voids that form during NiO reduction.

The statistical similarity of the properties of the samples reduced via each method indicates that planar, Ni-GDC/GDC based SOFC ASL and half-cells are able to be safely reduced, cooled, and handled in ambient conditions without leading to damaging re-oxidation of the nickel anode material. This resilience could enable some degree of large-batch reduction of cell anodes prior to SOFC stack assembly, leading to more rapid startup and a greater degree of sealing control.

3.4   Conclusions

A temperature and atmosphere controlled three-point bend fixture was designed and built for use in a universal testing machine. SOFC coupons and component materials were evaluated for flexural strength at room temperature and IT-SOFC operating temperatures. In addition, the effects of porosity percent and pore geometry on flexural strength in GDC were investigated. Furthermore, the impact of temperature on the reduction rate of NiO in NiO-GDC SOFC anodes was examined along with the resilience to re-oxidation at ambient conditions of this SOFC component.

Pore geometry had a significant impact on the flexural strength of GDC10, with spherical pores showing the greatest resistance to fracture. This supports the concept of pores acting as the new crack tip once a crack has advanced to the pore. Additionally, samples tested at $650\,^\circ$C were stronger than those at room temperature.
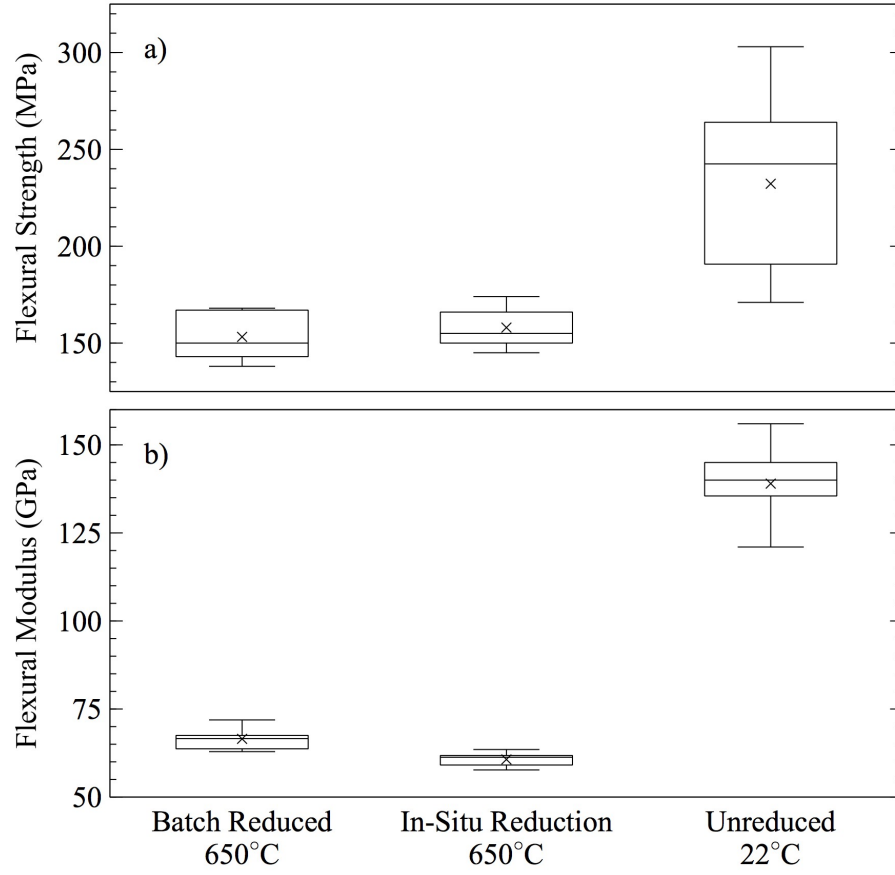
Figure 3.10: Flexural properties, a) strength and b) modulus, of Ni-GDC/GDC half-cell coupons after reduction via two different methods, compared to unreduced cells. Strength and modulus show decrease upon reduction but no significant difference between methods.

This is likely due to localized compressive stresses from thermal expansion of the material. This hypothesis is further supported by the results of testing NiO-GDC anode support coupons and half-cells. Coupons tested at $25\,°C$, $450\,°C$, and $650\,°C$ displayed a linear strength dependence with temperature. There was no statistical difference in strength between anode support layers and half-cells composed of anode support and electrolyte at a given temperature in air. Half-cells in which NiO was reduced to Ni by exposure to H_2 at $650\,°C$ displayed significant differences in strength when the electrolyte layer was subjected to compressive stress as opposed to tensile stress. Placing the ceramic electrolyte in compression and the metal-ceramic composite anode in tension resulted in the highest strength.

The reduction temperature of NiO-GDC/GDC half-cells was shown to have an effect on the rate of NiO reduction and amount of NiO reduced. At lower temperatures, the oxidation rate of Ni-GDC is slow enough that the anode can be exposed to air for significant periods below $100\,°C$. Any re-oxidation, combined with the cooling and re-heating of a cell back to $650\,°C$, showed no effect on the mechanical properties when compared to cells which had been reduced in-situ at $650\,°C$. These results indicate that it is possible to reduce and cool cell components to an extent without any additional effects to mechanical properties, allowing for more flexibility during cell manufacturing, stack assembly, and with quality control screenings.

This work leads to three important conclusions for the mechanical properties of GDC-based SOFCs using Ni anodes. Porous GDC used in anode supported SOFCs should be fabricated such that the pore geometry is spherical as this maximizes

energy required to advance a crack through the ceramic. Care should be taken in stack construction to ensure any out-of-plane cells are placed to compress the electrolyte and place the reduced anode in tension so as to lower the chance of fracture. Finally, it is possible to reduce the anodes of Ni-GDC SOFCs and then handle them at ambient conditions for quality control and stack assembly. This will remove a degree of variability from the manufacture of cells and stacks.

Appendix A: Statistics

A.1   Student's t-test

Lorem ipsum dolor sit amet, consectetuer adipiscing elit. Ut purus elit, vestibulum ut, placerat ac, adipiscing vitae, felis. Curabitur dictum gravida mauris. Nam arcu libero, nonummy eget, consectetuer id, vulputate a, magna. Donec vehicula augue eu neque. Pellentesque habitant morbi tristique senectus et netus et malesuada fames ac turpis egestas. Mauris ut leo. Cras viverra metus rhoncus sem. Nulla et lectus vestibulum urna fringilla ultrices. Phasellus eu tellus sit amet tortor gravida placerat. Integer sapien est, iaculis in, pretium quis, viverra ac, nunc. Praesent eget sem vel leo ultrices bibendum. Aenean faucibus. Morbi dolor nulla, malesuada eu, pulvinar at, mollis ac, nulla. Curabitur auctor semper nulla. Donec varius orci eget risus. Duis nibh mi, congue eu, accumsan eleifend, sagittis quis, diam. Duis eget orci sit amet orci dignissim rutrum.

Nam dui ligula, fringilla a, euismod sodales, sollicitudin vel, wisi. Morbi auctor lorem non justo. Nam lacus libero, pretium at, lobortis vitae, ultricies et, tellus. Donec aliquet, tortor sed accumsan bibendum, erat ligula aliquet magna, vitae ornare odio metus a mi. Morbi ac orci et nisl hendrerit mollis. Suspendisse ut massa. Cras nec ante. Pellentesque a nulla. Cum sociis natoque penatibus et

magnis dis parturient montes, nascetur ridiculus mus. Aliquam tincidunt urna. Nulla ullamcorper vestibulum turpis. Pellentesque cursus luctus mauris.

Nulla malesuada porttitor diam. Donec felis erat, congue non, volutpat at, tincidunt tristique, libero. Vivamus viverra fermentum felis. Donec nonummy pellentesque ante. Phasellus adipiscing semper elit. Proin fermentum massa ac quam. Sed diam turpis, molestie vitae, placerat a, molestie nec, leo. Maecenas lacinia. Nam ipsum ligula, eleifend at, accumsan nec, suscipit a, ipsum. Morbi blandit ligula feugiat magna. Nunc eleifend consequat lorem. Sed lacinia nulla vitae enim. Pellentesque tincidunt purus vel magna. Integer non enim. Praesent euismod nunc eu purus. Donec bibendum quam in tellus. Nullam cursus pulvinar lectus. Donec et mi. Nam vulputate metus eu enim. Vestibulum pellentesque felis eu massa.

Quisque ullamcorper placerat ipsum. Cras nibh. Morbi vel justo vitae lacus tincidunt ultrices. Lorem ipsum dolor sit amet, consectetuer adipiscing elit. In hac habitasse platea dictumst. Integer tempus convallis augue. Etiam facilisis. Nunc elementum fermentum wisi. Aenean placerat. Ut imperdiet, enim sed gravida sollicitudin, felis odio placerat quam, ac pulvinar elit purus eget enim. Nunc vitae tortor. Proin tempus nibh sit amet nisl. Vivamus quis tortor vitae risus porta vehicula.

Fusce mauris. Vestibulum luctus nibh at lectus. Sed bibendum, nulla a faucibus semper, leo velit ultricies tellus, ac venenatis arcu wisi vel nisl. Vestibulum diam. Aliquam pellentesque, augue quis sagittis posuere, turpis lacus congue quam, in hendrerit risus eros eget felis. Maecenas eget erat in sapien mattis porttitor. Vestibulum porttitor. Nulla facilisi. Sed a turpis eu lacus commodo facilisis. Morbi

fringilla, wisi in dignissim interdum, justo lectus sagittis dui, et vehicula libero dui cursus dui. Mauris tempor ligula sed lacus. Duis cursus enim ut augue. Cras ac magna. Cras nulla. Nulla egestas. Curabitur a leo. Quisque egestas wisi eget nunc. Nam feugiat lacus vel est. Curabitur consectetuer.

Suspendisse vel felis. Ut lorem lorem, interdum eu, tincidunt sit amet, laoreet vitae, arcu. Aenean faucibus pede eu ante. Praesent enim elit, rutrum at, molestie non, nonummy vel, nisl. Ut lectus eros, malesuada sit amet, fermentum eu, sodales cursus, magna. Donec eu purus. Quisque vehicula, urna sed ultricies auctor, pede lorem egestas dui, et convallis elit erat sed nulla. Donec luctus. Curabitur et nunc. Aliquam dolor odio, commodo pretium, ultricies non, pharetra in, velit. Integer arcu est, nonummy in, fermentum faucibus, egestas vel, odio.

Sed commodo posuere pede. Mauris ut est. Ut quis purus. Sed ac odio. Sed vehicula hendrerit sem. Duis non odio. Morbi ut dui. Sed accumsan risus eget odio. In hac habitasse platea dictumst. Pellentesque non elit. Fusce sed justo eu urna porta tincidunt. Mauris felis odio, sollicitudin sed, volutpat a, ornare ac, erat. Morbi quis dolor. Donec pellentesque, erat ac sagittis semper, nunc dui lobortis purus, quis congue purus metus ultricies tellus. Proin et quam. Class aptent taciti sociosqu ad litora torquent per conubia nostra, per inceptos hymenaeos. Praesent sapien turpis, fermentum vel, eleifend faucibus, vehicula eu, lacus.

A.2   Weibull Statistics

.

Lorem ipsum dolor sit amet, consectetuer adipiscing elit. Ut purus elit, vestibulum ut, placerat ac, adipiscing vitae, felis. Curabitur dictum gravida mauris. Nam arcu libero, nonummy eget, consectetuer id, vulputate a, magna. Donec vehicula augue eu neque. Pellentesque habitant morbi tristique senectus et netus et malesuada fames ac turpis egestas. Mauris ut leo. Cras viverra metus rhoncus sem. Nulla et lectus vestibulum urna fringilla ultrices. Phasellus eu tellus sit amet tortor gravida placerat. Integer sapien est, iaculis in, pretium quis, viverra ac, nunc. Praesent eget sem vel leo ultrices bibendum. Aenean faucibus. Morbi dolor nulla, malesuada eu, pulvinar at, mollis ac, nulla. Curabitur auctor semper nulla. Donec varius orci eget risus. Duis nibh mi, congue eu, accumsan eleifend, sagittis quis, diam. Duis eget orci sit amet orci dignissim rutrum.

Nam dui ligula, fringilla a, euismod sodales, sollicitudin vel, wisi. Morbi auctor lorem non justo. Nam lacus libero, pretium at, lobortis vitae, ultricies et, tellus. Donec aliquet, tortor sed accumsan bibendum, erat ligula aliquet magna, vitae ornare odio metus a mi. Morbi ac orci et nisl hendrerit mollis. Suspendisse ut massa. Cras nec ante. Pellentesque a nulla. Cum sociis natoque penatibus et magnis dis parturient montes, nascetur ridiculus mus. Aliquam tincidunt urna. Nulla ullamcorper vestibulum turpis. Pellentesque cursus luctus mauris.

Nulla malesuada porttitor diam. Donec felis erat, congue non, volutpat at, tincidunt tristique, libero. Vivamus viverra fermentum felis. Donec nonummy pellentesque ante. Phasellus adipiscing semper elit. Proin fermentum massa ac quam. Sed diam turpis, molestie vitae, placerat a, molestie nec, leo. Maecenas lacinia. Nam ipsum ligula, eleifend at, accumsan nec, suscipit a, ipsum. Morbi

blandit ligula feugiat magna. Nunc eleifend consequat lorem. Sed lacinia nulla vitae enim. Pellentesque tincidunt purus vel magna. Integer non enim. Praesent euismod nunc eu purus. Donec bibendum quam in tellus. Nullam cursus pulvinar lectus. Donec et mi. Nam vulputate metus eu enim. Vestibulum pellentesque felis eu massa.

Quisque ullamcorper placerat ipsum. Cras nibh. Morbi vel justo vitae lacus tincidunt ultrices. Lorem ipsum dolor sit amet, consectetuer adipiscing elit. In hac habitasse platea dictumst. Integer tempus convallis augue. Etiam facilisis. Nunc elementum fermentum wisi. Aenean placerat. Ut imperdiet, enim sed gravida sollicitudin, felis odio placerat quam, ac pulvinar elit purus eget enim. Nunc vitae tortor. Proin tempus nibh sit amet nisl. Vivamus quis tortor vitae risus porta vehicula.

Fusce mauris. Vestibulum luctus nibh at lectus. Sed bibendum, nulla a faucibus semper, leo velit ultricies tellus, ac venenatis arcu wisi vel nisl. Vestibulum diam. Aliquam pellentesque, augue quis sagittis posuere, turpis lacus congue quam, in hendrerit risus eros eget felis. Maecenas eget erat in sapien mattis porttitor. Vestibulum porttitor. Nulla facilisi. Sed a turpis eu lacus commodo facilisis. Morbi fringilla, wisi in dignissim interdum, justo lectus sagittis dui, et vehicula libero dui cursus dui. Mauris tempor ligula sed lacus. Duis cursus enim ut augue. Cras ac magna. Cras nulla. Nulla egestas. Curabitur a leo. Quisque egestas wisi eget nunc. Nam feugiat lacus vel est. Curabitur consectetuer.

Suspendisse vel felis. Ut lorem lorem, interdum eu, tincidunt sit amet, laoreet vitae, arcu. Aenean faucibus pede eu ante. Praesent enim elit, rutrum at, molestie non, nonummy vel, nisl. Ut lectus eros, malesuada sit amet, fermentum eu, sodales

cursus, magna. Donec eu purus. Quisque vehicula, urna sed ultricies auctor, pede lorem egestas dui, et convallis elit erat sed nulla. Donec luctus. Curabitur et nunc. Aliquam dolor odio, commodo pretium, ultricies non, pharetra in, velit. Integer arcu est, nonummy in, fermentum faucibus, egestas vel, odio.

Sed commodo posuere pede. Mauris ut est. Ut quis purus. Sed ac odio. Sed vehicula hendrerit sem. Duis non odio. Morbi ut dui. Sed accumsan risus eget odio. In hac habitasse platea dictumst. Pellentesque non elit. Fusce sed justo eu urna porta tincidunt. Mauris felis odio, sollicitudin sed, volutpat a, ornare ac, erat. Morbi quis dolor. Donec pellentesque, erat ac sagittis semper, nunc dui lobortis purus, quis congue purus metus ultricies tellus. Proin et quam. Class aptent taciti sociosqu ad litora torquent per conubia nostra, per inceptos hymenaeos. Praesent sapien turpis, fermentum vel, eleifend faucibus, vehicula eu, lacus.

Appendix B: TGA Manual

B.1   Theory of Operation

Thermogravimetry works on the principle of measuring small changes in mass as the environment changes. Changes in environment can come from

B.2   Mass Measurement

The TGA uses a Cahn D200 microbalance for the mass sensing capability.

B.3   Gas Delivery

MKS Controllers are used.

B.4   pO$_2$ Measurement

Home built YSZ sensor.

B.5   Controls

Lab view on the computer.

B.6 Interfacing with other devices

Can be plumbed up to mass spec.

Lorem ipsum dolor sit amet, consectetuer adipiscing elit. Ut purus elit, vestibulum ut, placerat ac, adipiscing vitae, felis. Curabitur dictum gravida mauris. Nam arcu libero, nonummy eget, consectetuer id, vulputate a, magna. Donec vehicula augue eu neque. Pellentesque habitant morbi tristique senectus et netus et malesuada fames ac turpis egestas. Mauris ut leo. Cras viverra metus rhoncus sem. Nulla et lectus vestibulum urna fringilla ultrices. Phasellus eu tellus sit amet tortor gravida placerat. Integer sapien est, iaculis in, pretium quis, viverra ac, nunc. Praesent eget sem vel leo ultrices bibendum. Aenean faucibus. Morbi dolor nulla, malesuada eu, pulvinar at, mollis ac, nulla. Curabitur auctor semper nulla. Donec varius orci eget risus. Duis nibh mi, congue eu, accumsan eleifend, sagittis quis, diam. Duis eget orci sit amet orci dignissim rutrum.

Nam dui ligula, fringilla a, euismod sodales, sollicitudin vel, wisi. Morbi auctor lorem non justo. Nam lacus libero, pretium at, lobortis vitae, ultricies et, tellus. Donec aliquet, tortor sed accumsan bibendum, erat ligula aliquet magna, vitae ornare odio metus a mi. Morbi ac orci et nisl hendrerit mollis. Suspendisse ut massa. Cras nec ante. Pellentesque a nulla. Cum sociis natoque penatibus et magnis dis parturient montes, nascetur ridiculus mus. Aliquam tincidunt urna. Nulla ullamcorper vestibulum turpis. Pellentesque cursus luctus mauris.

Nulla malesuada porttitor diam. Donec felis erat, congue non, volutpat at, tincidunt tristique, libero. Vivamus viverra fermentum felis. Donec nonummy

pellentesque ante. Phasellus adipiscing semper elit. Proin fermentum massa ac quam. Sed diam turpis, molestie vitae, placerat a, molestie nec, leo. Maecenas lacinia. Nam ipsum ligula, eleifend at, accumsan nec, suscipit a, ipsum. Morbi blandit ligula feugiat magna. Nunc eleifend consequat lorem. Sed lacinia nulla vitae enim. Pellentesque tincidunt purus vel magna. Integer non enim. Praesent euismod nunc eu purus. Donec bibendum quam in tellus. Nullam cursus pulvinar lectus. Donec et mi. Nam vulputate metus eu enim. Vestibulum pellentesque felis eu massa.

Quisque ullamcorper placerat ipsum. Cras nibh. Morbi vel justo vitae lacus tincidunt ultrices. Lorem ipsum dolor sit amet, consectetuer adipiscing elit. In hac habitasse platea dictumst. Integer tempus convallis augue. Etiam facilisis. Nunc elementum fermentum wisi. Aenean placerat. Ut imperdiet, enim sed gravida sollicitudin, felis odio placerat quam, ac pulvinar elit purus eget enim. Nunc vitae tortor. Proin tempus nibh sit amet nisl. Vivamus quis tortor vitae risus porta vehicula.

Fusce mauris. Vestibulum luctus nibh at lectus. Sed bibendum, nulla a faucibus semper, leo velit ultricies tellus, ac venenatis arcu wisi vel nisl. Vestibulum diam. Aliquam pellentesque, augue quis sagittis posuere, turpis lacus congue quam, in hendrerit risus eros eget felis. Maecenas eget erat in sapien mattis porttitor. Vestibulum porttitor. Nulla facilisi. Sed a turpis eu lacus commodo facilisis. Morbi fringilla, wisi in dignissim interdum, justo lectus sagittis dui, et vehicula libero dui cursus dui. Mauris tempor ligula sed lacus. Duis cursus enim ut augue. Cras ac magna. Cras nulla. Nulla egestas. Curabitur a leo. Quisque egestas wisi eget nunc. Nam feugiat lacus vel est. Curabitur consectetuer.

Suspendisse vel felis. Ut lorem lorem, interdum eu, tincidunt sit amet, laoreet vitae, arcu. Aenean faucibus pede eu ante. Praesent enim elit, rutrum at, molestie non, nonummy vel, nisl. Ut lectus eros, malesuada sit amet, fermentum eu, sodales cursus, magna. Donec eu purus. Quisque vehicula, urna sed ultricies auctor, pede lorem egestas dui, et convallis elit erat sed nulla. Donec luctus. Curabitur et nunc. Aliquam dolor odio, commodo pretium, ultricies non, pharetra in, velit. Integer arcu est, nonummy in, fermentum faucibus, egestas vel, odio.

Sed commodo posuere pede. Mauris ut est. Ut quis purus. Sed ac odio. Sed vehicula hendrerit sem. Duis non odio. Morbi ut dui. Sed accumsan risus eget odio. In hac habitasse platea dictumst. Pellentesque non elit. Fusce sed justo eu urna porta tincidunt. Mauris felis odio, sollicitudin sed, volutpat a, ornare ac, erat. Morbi quis dolor. Donec pellentesque, erat ac sagittis semper, nunc dui lobortis purus, quis congue purus metus ultricies tellus. Proin et quam. Class aptent taciti sociosqu ad litora torquent per conubia nostra, per inceptos hymenaeos. Praesent sapien turpis, fermentum vel, eleifend faucibus, vehicula eu, lacus.

Appendix C: Code

C.1 Arduino PID Relay Furnace Controller with Serial Connectivity

The purpose of this Arduino sketch is to power a heating furnace (controlled by a relay), with PID controls. In addition serial communications are added to monitor, log, and interact with the controller.

C.1.1 Hardware and other libraries

This was built to be used on a Arduino Uno R3, but should be easily run on a variety of different boards. For temperature sensing, an Adafruit MAX31856 is used with the library from them. Also used is the PID controller library by br3ttb. All I have really done is put the two together with the ability to communicate over serial.

C.1.2 Variables

Here are a list of variables for things you may want to change based on your setup.

- RelayPin: The physical pin your relay is connected to.

- Adafruit_MAX31856(CS, DI, DO, CLK): Pins for your MAX31856

- WindowSize: Length of on/off cycle, needed to account for AC power

- printdelay: Delay time in milliseconds for printout on serial

- MaxOP: Maximum operating power, used to extend life of elements

- myPID(&Input, &Output, &workingSet,P,I,D, DIRECT): PID need to be adjusted for your setup. If inverse behavior is experienced (e.g. heats when it should cool) switch DIRECT.

- workingSet and Setpoint: Inital setpoint for power on

- ramprate: Sets a ramp rate for the working setpoint. Measured in milliseconds for 1C change.

C.1.3 Serial communications

Baud rate is set to 9600. Output is tab deliminated of Setpoint, Working Setpoint, Thermocouple Temperature, and Output Power. To change set point, send a new number over serial and press return. You may have to adjust your serial monitor to send \n as end of line.

```
1 #include <Adafruit_MAX31856.h> //loads library for thermocouple reader
2 #include <PID_v1.h> //loads PID library
3 #include <RunningAverage.h> //loads class for Running Avgerage
      ↪ calculations
4 #define RelayPin 2 //set pin number which is connected to power relay
      ↪ for device
5
```

```
6  const byte numChars = 32;

7  char receivedChars[numChars]; // an array to store the received data

8

9  boolean newData = false; //trigger to determine if data needs to be
       ↪ read

10

11 Adafruit_MAX31856 max = Adafruit_MAX31856(4, 5, 6, 7); // Software SPI,
       ↪  Pin number for: CS, DI, DO, CLK

12

13 //Define Variables

14 double workingSet, Setpoint, Input, Output;

15 int WindowSize = 1000; //Length of cycle for power on/off

16 unsigned long prevprintMillis = 0;

17 const long printdelay = 5000; //delay amount before printing via serial

18 unsigned long windowStartTime;

19 unsigned long prevRampTimer = 0;

20 unsigned long MaxOP = .95; // Max Operating Power

21

22 RunningAverage myRA(10); //Set up running average with # of
       ↪ measurements

23

24 PID myPID(&Input, &Output, &workingSet,250,50,8, DIRECT); //Specify the
       ↪  links and initial tuning parameters

25

26 void setup() {

27   pinMode(RelayPin, OUTPUT); //define RelayPin as an output

28
```

62

```
29    //staring serial communications
30    Serial.begin(9600);
31    Serial.println("PID Controller Output");
32    Serial.println("Setpoint\t Working SP\t TC Temp\t Output");//tab
         ↪ deliminated for logging
33
34    //setup for thermocouple reader
35    max.begin();
36    max.setThermocoupleType(MAX31856_TCTYPE_K);//change type if needed
37
38    windowStartTime = millis(); //start timer for duty cycle window
39
40    myRA.clear(); // explicitly start clean
41
42    //initialize the variables we're linked to
43    workingSet = 20;
44    Setpoint = 20;
45
46    myPID.SetOutputLimits(0, MaxOP * WindowSize); //tell the PID to range
         ↪  between 0 and the full window size
47    myPID.SetMode(AUTOMATIC);   //turn the PID on
48
49 }
50
51 //fuction to recieve data via serial and process when endmarker is
       ↪ recieved
52 void recvWithEndMarker() {
```

```
53   static byte ndx = 0;

54   char endMarker = '\n'; //define line endmarker for client

55   char rc;

56

57   // if (Serial.available() > 0) {

58    while (Serial.available() > 0 && newData == false) {

59      rc = Serial.read();

60

61      if (rc != endMarker) {

62        receivedChars[ndx] = rc;

63        ndx++;

64        if (ndx >= numChars) {

65          ndx = numChars − 1;

66        }

67      }

68      else {

69        receivedChars[ndx] = '\0'; // terminate the string

70        ndx = 0;

71        newData = true;

72      }

73    }

74 }

75

76 //Function to repeat new setpoint for confirmation

77 void showNewData() {

78   if (newData == true) {

79   String recievedString = String(receivedChars);
```

```arduino
80    Serial.print("Setpoint changed to ... ");

81    Serial.println(recievedString.toFloat());

82    Setpoint = recievedString.toFloat();

83    newData = false;

84    }

85  }

86

87  void loop() {

88    recvWithEndMarker(); //check for new setpoint

89    showNewData(); //sets new setpoint and displays it

90

91  //   Input = max.readThermocoupleTemperature(); //read thermocouple

92

93    myRA.addValue(max.readThermocoupleTemperature());

94

95    Input = myRA.getAverage();

96

97    myPID.Compute(); //calculate PID output

98

99  //print delay for serial output so not to flood logs

100   unsigned long printMillis = millis();

101   if (printMillis - prevprintMillis >= printdelay) {

102     prevprintMillis = printMillis;

103     Serial.print(Setpoint); Serial.print("\t"); Serial.print(workingSet);
      ↪ Serial.print("\t"); Serial.print(max.readThermocoupleTemperature
      ↪ ()); Serial.print("\t"); Serial.println(Output/WindowSize*100);

104   }
```

```
105
106 //turn the output pin on/off based on pid output
107   if (millis() - windowStartTime>=WindowSize)
108    { //time to shift the Relay Window
109       windowStartTime += WindowSize;
110    }
111   if (Output < millis() - windowStartTime) digitalWrite(RelayPin,LOW); //
          ↪ HIGH and LOW set to default off
112    else digitalWrite(RelayPin,HIGH);
113
114 //sets ramp rate functionality
115 unsigned long ramptimer = millis();
116 unsigned long ramprate = 6000;//milliseconds for 1C change
117   if (workingSet != Setpoint)
118   {
119     if (ramptimer - prevRampTimer >= ramprate && workingSet < Setpoint)
120     {
121      workingSet++;
122      prevRampTimer = ramptimer;
123     }
124     if (ramptimer - prevRampTimer >= ramprate && workingSet > Setpoint)
125     {
126      workingSet--;
127      prevRampTimer = ramptimer;
128     }
129   }
130 }
```

Bibliography

[1] U.S. Energy Information Administration. World energy demand and economic outlook. Technical Report May 2016, U.S. Energy Information Administration, 2016.

[2] Stephen G Osborn, Avner Vengosh, Nathaniel R Warner, and Robert B Jackson. Methane contamination of drinking water accompanying gas-well drilling and hydraulic fracturing. *Proceedings of the National Academy of Sciences of the United States of America*, 108(20):8172–6, 2011.

[3] Avner Vengosh, Robert B Jackson, Nathaniel Warner, Thomas H Darrah, and Andrew Kondash. A Critical Review of the Risks to Water Resources from Shale Gas Development and Hydraulic Fracturing in the United States. *Environmental Science & Technology*, 16(4):6838, 2014.

[4] Susan Solomon, Gian-Kasper Plattner, Reto Knutti, and Pierre Friedlingstein. Irreversible climate change due to carbon dioxide emissions. *Proceedings of the National Academy of Sciences of the United States of America*, 106(6):1704–9, 2009.

[5] J Hansen, D Johnson, a Lacis, S Lebedeff, P Lee, D Rind, and G Russell. Climate impact of increasing atmospheric carbon dioxide. *Science (New York, N.Y.)*, 213(4511):957–966, 1981.

[6] U.S. Environmental Protection Agency. Inventory of U.S. Greenhouse Gas Emissions and Sinks: 1990 - 2015. Technical report, U.S. Environmental Protection Agency, 2017.

[7] E. D. Wachsman and K. T. Lee. Lowering the Temperature of Solid Oxide Fuel Cells. *Science*, 334(6058):935–939, 2011.

[8] Robert H. Lasseter and Paolo Paigi. Microgrid: A conceptual solution. *PESC Record - IEEE Annual Power Electronics Specialists Conference*, 6:4285–4290, 2004.

[9] Seungdoo Park, John M. Vohs, and Raymond J. Gorte. Direct oxidation of hydrocarbons in a solid-oxide fuel cell. *Nature*, 404(6775):265–267, 2000.

[10] Nguyen Q. Minh. Solid oxide fuel cell technology - Features and applications. *Solid State Ionics*, 174(1-4):271–277, 2004.

[11] Wikimedia Commons. Solid Oxide Fuel Cell Diagram.

[12] Mogens Mogensen, Nigel M. Sammes, and Geoff A. Tompsett. Physical, chemical and electrochemical properties of pure and doped ceria. *Solid State Ionics*, 129(1):63–94, 2000.

[13] James Larminie and Andrew Dicks. *Fuel Cell Systems Explained*, volume 93. 2001.

[14] I. Pilatowsky, R.J. Romero, C.A. Isaza, S.A. Gamboa, P.J. Sebastian, and W. Rivera. Thermodynamics of Fuel Cells. In *Cogeneration Fuel Cell- Sorption Air Conditioning Systems*, pages 25–37. 2008.

[15] Mikko Pihlatie, Andreas Kaiser, and Mogens Mogensen. Mechanical properties of NiO/Ni-YSZ composites depending on temperature, porosity and redox cycling. *Journal of the European Ceramic Society*, 29(9):1657–1664, 2009.

[16] J. Laurencin, G. Delette, O. Sicardy, S. Rosini, and F. Lefebvre-Joud. Impact of 'redox' cycles on performances of solid oxide fuel cells: Case of the electrolyte supported cells. *Journal of Power Sources*, 195(9):2747–2753, 2010.

[17] Jiang Liu, Brian D Madsen, Zhiqiang Ji, and Scott A Barnett. A Fuel-Flexible Ceramic-Based Anode for Solid Oxide Fuel Cells. *Electrochemical and Solid-State Letters*, 5(May 2012):122–124, 2002.

[18] Sossina M. Haile. Fuel cell materials and components. *Acta Materialia*, 51(19):5981–6000, 2003.

[19] Harumi Yokokawa, Hengyong Tu, Boris Iwanschitz, and Andreas Mai. Fundamental mechanisms limiting solid oxide fuel cell durability. *Journal of Power Sources*, 182(2):400–412, 2008.

[20] F. Gutierrez-Mora, J. M. Ralph, and J. L. Routbort. High-temperature mechanical properties of anode-supported bilayers. *Solid State Ionics*, 149(3-4):177–184, 2002.

[21] Ji Haeng Yu, Gun Woo Park, Shiwoo Lee, and Sang Kuk Woo. Microstructural effects on the electrical and mechanical properties of Ni-YSZ cermet for SOFC anode. *Journal of Power Sources*, 163(2):926–932, 2007.

[22] William D. Callister and David G. Rethwisch. Influence of Porosity. In *Materials Science and Engineering: An Introduction*, pages 373–381. 2014.

[23] Michel Barsoum. Processing and Surface Flaws. In *Fundamentals of Ceramics*, pages 374–381. 2003.

[24] John B. Goodenough and Yun Hui Huang. Alternative anode materials for solid oxide fuel cells. *Journal of Power Sources*, 173(1):1–10, 2007.

[25] Shaowu Zha, Philip Tsang, Zhe Cheng, and Meilin Liu. Electrical properties and sulfur tolerance of La0.75Sr 0.25Cr1-xMnxO3 under anodic conditions. *Journal of Solid State Chemistry*, 178(6):1844–1850, 2005.

[26] S. Primdahl, J. R. Hansen, L. Grahl-Madsen, and P. H. Larsen. Sr-Doped LaCrO[sub 3] Anode for Solid Oxide Fuel Cells. *Journal of The Electrochemical Society*, 148(1):A74, 2001.

[27] A. Mohammed Hussain, Jens V.T. Høgh, Wei Zhang, Peter Blennow, Nikolaos Bonanos, and Bernard A. Boukamp. Effective improvement of interface modified strontium titanate based solid oxide fuel cell anodes by infiltration with nano-sized palladium and gadolinium-doped cerium oxide. *Electrochimica Acta*, 113:635–643, 2013.

[28] A. Mohammed Hussain, Jens V.T. Høgh, Torben Jacobsen, and Nikolaos Bonanos. Nickel-ceria infiltrated Nb-doped SrTiO3for low temperature SOFC anodes and analysis on gas diffusion impedance. *International Journal of Hydrogen Energy*, 37(5):4309–4318, 2012.

[29] A. Mohammed Hussain, Ke-Ji Pan, Ian A. Robinson, Thomas Hays, and Eric D. Wachsman. Stannate-Based Ceramic Oxide as Anode Materials for Oxide-Ion Conducting Low-Temperature Solid Oxide Fuel Cells. *Journal of The Electrochemical Society*, 163(10):F1198–F1205, 2016.

[30] Yun-Hui Huang, Ronald I Dass, Zheng-Liang Xing, and John B Goodenough. Double Perovskites as Anode Materials for Solid-Oxide Fuel Cells. *Science*, 2(April):254–258, 2006.

[31] S.H Chan, K.a Khor, and Z.T Xia. A complete polarization model of a solid oxide fuel cell and its sensitivity to the change of cell component thickness. *Journal of Power Sources*, 93(1-2):130–140, 2001.

[32] Felix Fleischhauer, Andreas Tiefenauer, Thomas Graule, Robert Danzer, Andreas Mai, and Jakob Kuebler. Failure analysis of electrolyte-supported solid oxide fuel cells. *Journal of Power Sources*, 258:382–390, 2014.

[33] J. Laurencin, G. Delette, F. Lefebvre-Joud, and M. Dupeux. A numerical tool to estimate SOFC mechanical degradation: Case of the planar cell configuration. *Journal of the European Ceramic Society*, 28(9):1857–1869, 2008.

[34] S.R. Bishop, D. Marrocchelli, C. Chatzichristodoulou, N.H. Perry, M.B. Mogensen, H.L. Tuller, and E.D. Wachsman. Chemical Expansion: Implications

for Electrochemical Energy Storage and Conversion Devices. *Annual Review of Materials Research*, 44(1):205–239, 2014.

[35] Keith L. Duncan, Yanli Wang, Sean R. Bishop, Fereshteh Ebrahimi, and Eric D. Wachsman. Role of point defects in the physical properties of fluorite oxides. *Journal of the American Ceramic Society*, 89(10):3162–3166, 2006.

[36] Yanli Wang, Keith Duncan, Eric D. Wachsman, and Fereshteh Ebrahimi. The effect of oxygen vacancy concentration on the elastic modulus of fluorite-structured oxides. *Solid State Ionics*, 178(1-2):53–58, 2007.

[37] M. Jenkins, T. Chang, and A. Okura. A Simple Maching Jig for Chevron-notched Specimens. *Experimental Techniques*, 12(8):20–22, 1988.

[38] ASTM. Standard Test Methods for Determination of Fracture Toughness of Advanced Ceramics. pages 1–33, 2016.

[39] ASTM. Standard Test Method for Flexural Strength of Advanced Ceramics at Ambient. *Annual Book of ASTM Standards*, 11(Reapproved 2008):1–16, 2013.

[40] Brian H Toby and Robert B Von Dreele. GSAS-II : the genesis of a modern open-source all purpose crystallography software package. pages 544–549, 2013.

[41] Koichi Momma and Fujio Izumi. VESTA 3 for three-dimensional visualization of crystal, volumetric and morphology data. *Journal of Applied Crystallography*, 44(6):1272–1276, 2011.

[42] Shang Xian Wu. Fracture toughness determination of bearing steel using chevron-notch three point bend specimen. *Engineering Fracture Mechanics*, 19(2):221–232, 1984.

[43] Jeongpill Ki and Daejong Kim. Computational model to predict thermal dynamics of planar solid oxide fuel cell stack during start-up process. *Journal of Power Sources*, 195(10):3186–3200, 2010.

[44] J. J. Roa, M. A. Laguna-Bercero, A. Larrea, V. M. Orera, and M. Segarra. Mechanical properties of highly textured porous Ni-YSZ and Co-YSZ cermets produced from directionally solidified eutectics. *Ceramics International*, 37(8):3123–3131, 2011.

[45] Arata Nakajo, Jakob Kuebler, Antonin Faes, Ulrich F. Vogt, Hans Jürgen Schindler, Lieh Kwang Chiang, Stefano Modena, Jan Van Herle, and Thomas Hocker. Compilation of mechanical properties for the structural analysis of solid oxide fuel cell stacks. Constitutive materials of anode-supported cells. *Ceramics International*, 38(5):3907–3927, 2012.

[46] Zhen Yan Deng, Jihong She, Yoshiaki Inagaki, Jian Feng Yang, Tatsuki Ohji, and Yoshihisa Tanaka. Reinforcement by crack-tip blunting in porous ceramics. *Journal of the European Ceramic Society*, 24(7):2055–2059, 2004.

[47] Milan Ambrozic and Tomaz Kosmac. Optimization of the bend strength of flat-layered alumina-zirconia composites. *Journal of the American Ceramic Society*, 90(5):1545–1550, 2007.

[48] Akio Yonezu and Xi Chen. Micro-scale damage characterization in porous ceramics by an acoustic emission technique. *Ceramics International*, 40(7 PART A):9859–9866, 2014.

[49] S. Meille, M. Lombardi, J. Chevalier, and L. Montanaro. Mechanical properties of porous ceramics in compression: On the transition between elastic, brittle, and cellular behavior. *Journal of the European Ceramic Society*, 32(15):3959–3967, 2012.

[50] Pulin Nie, Heping Lv, Tao Zhou, Xun Cai, and Paul K. Chu. Interfacial adhesion measurement of a ceramic coating on metal substrate. *Journal of Coatings Technology Research*, 7(3):391–398, 2010.

[51] C Olagnon. Determination of the fracture mechanical parameters of porous ceramics from microstructure parameters measured by quantitative image analysis. *Journal of Materials Science*, 4(1):4081–4088, 1999.

[52] B. F. Sorensen and A. Horsewell. Crack Growth along Interfaces in Porous Ceramic Layers. *Journal of the American Ceramic Society*, 84(9):2051–59, 2001.

[53] S M Barinov, V F Ponomarev, and V Ya Shevchenko. Effect of Hot Isostatic Pressing on the Mechanical Properties of Aluminum Oxide Ceramics. pages 9–12, 1997.

[54] K Yasuda, K Uemura, and T Shiota. Sintering and mechanical properties of gadolinium-doped ceria ceramics. *Journal of Physics: Conference Series*, 339(1):012006, 2012.

[55] Roy W. Rice. *Porosity of Ceramics: Properties and Applications*. Marcel Dekker. Inc., New York, illustrate edition, 1998.

[56] Rodger W. Davidge and Anthony G. Evans. The Strength of Ceramics. *Materials Science and Engineering*, (6):281–298, 1970.

[57] Sophie Giraud and Jérôme Canel. Young's modulus of some SOFCs materials as a function of temperature. *Journal of the European Ceramic Society*, 28(1):77–83, 2008.

[58] Barry Carter and Grant Norton. *Ceramic Materials Science and Engineering*. 2007.

[59] Oldřich Ševeček, Michal Kotoul, Dominique Leguillon, Eric Martin, and Raul Bermejo. Assessment of crack-related problems in layered ceramics using the finite fracture mechanics and coupled stress-energy criterion. *Procedia Structural Integrity*, 2:2014–2021, 2016.

[60] James T Richardson, Robert Scates, and Martyn V Twigg. X-ray diffraction study of nickel oxide reduction by hydrogen. *Applied Catalysis A: General*, 246:137–150, 2003.